Academic year:

Acknowledgements

First and foremost, I would like to thank Prof. Dr. Macián-Juan for giving me the opportunity to write this thesis in the Nuclear Engineering department of TUM.

I would also like to express my deepest gratitude to Dipl. Ing. Andreas Wanninger for his commitment to this project. He has shown great patience and a positive attitude throughout these months, always giving good advice and assisting me when needed. I really wish him all the best for his scientific project and his future.

Many thanks to Prof. Juan Ignacio Cuadrado Iglesias for his help in readapting this thesis to the requirements of the UPV.

Special mention to my co-worker and friend Jaime Ruiz for his continuous support, his encouragement and positivity in the bad moments. It was a pleasure sharing this unforgettable experience in Munich and I'm sure these two years would have been very different without him.

Finally, I would like to thank my parents for always supporting me, even though they are far away. The opportunity of experiencing two years abroad wouldn't have been possible without them. They made the tough days during this time much better.

Erklärung

Hiermit versichere ich, die vorliegende Arbeit selbstständig und ohne Hilfe Dritter angefertigt zu haben. Gedanken und Zitate, die ich aus fremden Quellen direkt oder indirekt übernommen habe, sind als solche kenntlich gemacht. Diese Arbeit hat in gleicher oder ähnlicher Form noch keiner Prüfungsbehörde vorgelegen und wurde bisher nicht veröffentlicht.

Ich erkläre mich damit einverstanden, dass die Arbeit durch den Lehrstuhl für Nukleartechnik der Öffentlichkeit zugänglich gemacht werden kann.

This is the report of authenticity of the original Master Thesis work carried out under the Double Degree Program framework with the Technical Univeristy of Munich (TUM) in the academic year 2015-16.

München, den 30.08.16

Luis Rafecas

Abstract

The Fuel Assembly bow issue in Pressurized Water Reactors (PWRs) was first discovered in 1994 at Ringhals nuclear power plant (Sweden). Several problems concerning both, safety and operating performance, may arise as a consequence of excessive Fuel Assembly deformation.

Regarding the safety concern, geometry changes induced by the bending moments affecting FA can lead to Incomplete Rod Insertion (IRI). As the aim of the control rods is to control the fission chain reaction in the core, IRI events represent a threat in case of a loss of coolant accident or a quick shutdown situation.

In addition, FA deformation does also have an impact on the reactor's operating performance. The induced deformation causes irregular gap widths and uneven water gaps through which the coolant flows, leading to unequal thermal transfer and thus to a decrease in thermal margins. Moreover, the strong friction forces between assemblies extend core fueling and defueling times and may cause grid damage during shuffling of the Fuel Assemblies.

The fundamental role when it comes to excessive FA bowing is believed to be played by the influence of lateral hydrodynamic forces. Other factors such as irradiation induced creep deformation and excessive hold down spring forces also have to be taken into account when analyzing the bow issue.

Since the FA deformation is both, a performance and a safety concern, the prediction of its mechanical behavior has turned into an active field of research. Therefore, the improvement of bow modelling instruments, mainly based on Computational Fluid Dynamics (CFD) simulation, has become essential.

The objective of this thesis is the optimization of the model mesh which will best enable the most efficient, whilst still accurate, estimation of the lateral hydrodynamic forces inside the reactor core.

Meshes with different node densities are created (from 3472 nodes to 32144 nodes). A mesh independence study is carried out for a non-deformed and a C-shape deformed FA structure. The aim of comparing the results from both cases is to determine whether the condition of structural deformation has an influence on the results of the study and on the convergence of the simulations.

For both studies, the requirements of accuracy and few computational expense are better accomplished by the mesh consisting of 14340 nodes. At the same time, convergence is also achieved within a similar amount of iterations.

A porous model is selected to determine the lateral forces of an entire FA row, since simulating the entire core's behavior with respect to bow would be too computationally expensive and time consuming due to the complex geometries of a PWR.

Keywords: Fuel Assembly, bow phenomenon, PWR, Optimization study, mesh independence study, CFD, convergence

Table of contents

DOCUMENTS CONTAINED IN THIS MASTER THESIS:

- **Thesis Project**
- **Thesis Budget**

THESIS Project:

List of figures

List of figures

List of tables

List of acronyms

AMAE	Averaged Mean Absolute Error
BWR	Boiling Water Reactor
CCL	CFX Command Language
CFD	Computational Fluid Dynamics
FA	Fuel Assembly
FEM	Finite Element Method
FSI	Fuel Structure Interaction
IRI	Incomplete Rod Insertion
LWR	Light Water Reactor
MOX	Mixed Oxide Fuel
PDEs	Partial Differential Equations
PWR	Pressurized Water Reactor
QM	Quadratic Mean
RMS	Root Mean Square
SCWR	Supercritical Water Reactor
SG	Steam Generator

Thesis Project

1. Theoretical Framework of this Thesis

Fuel Assembly bow is a very concerning issue for nuclear power plants since it affects both, its safety and its operating performance. Bow of up to 20 mm has been observed in certain fuel designs. It is mainly represented by an S-shape (Figure 1) or a C-shape deformation of the Fuel Assemblies (Figure 2).
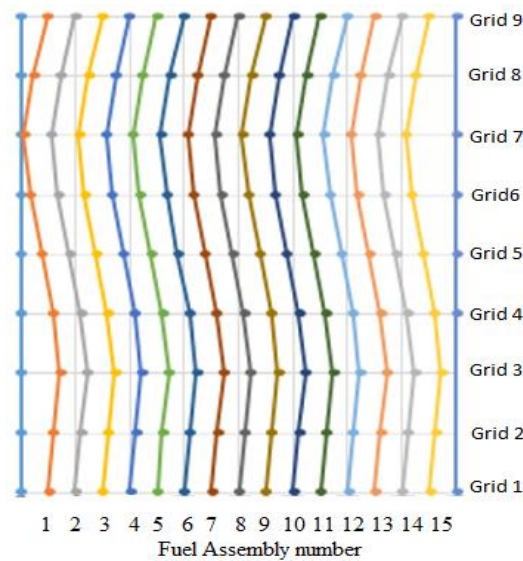
Figure 1: S-shape deformed Fuel Assembly row
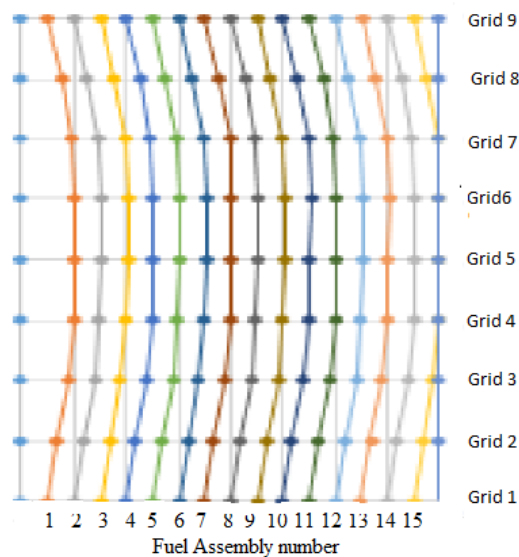
Figure 2: C-shape deformed Fuel Assembly row

The main cause of FA deformation is believed to be played by the influence of lateral hydrodynamic forces [1,3]. They are considered to be caused by the existing pressure gradients, which are generated by pressure drops in the reactor core.

Excessive hold-down spring forces do also contribute to FA deformation. The reactor core in PWRs is comprised of an array of square Fuel Assemblies. First, the FAs are placed on the lower core plate. Then, the upper core support structure containing the upper core plate is installed. This plate presses down the Fuel Assembly hold-down springs to hold the Fuel Assemblies in place against the upward hydraulic force, putting the Fuel Assemblies under compressive load [2], thus contributing to FA deformation.

Furthermore, irradiation growth leads to an increase in the FA length [2]. The irradiation growth is defined as a change in shape without a volume change during irradiation in the absence of applied stress. This triggers an increase in the compressive load of the hold-down spring forces, leading to more FA deformation.

The safety and operating performance of the PWRs is affected by several problems derived from FA deformation, such as increased rod drop time or by Incomplete Rod Insertion (IRI). Control rods are in charge of regulating the fission chain reaction inside the core, hence IRI events might be a serious threat concerning the safety of the power plant if a quick shutdown situation is required.

Structural deformation also leads to contact between neighboring Fuel Assemblies, consequently extending refueling and outage times and causing grid damage during shuffling of the Fuel Assemblies, resulting in higher costs [1]. Irregular gap widths between the Fuel Assemblies are another consequence of FA distortion. This causes unequal thermal heat transfer and thus a decrease in thermal efficiency.

Since the FA deformation is both, a performance and safety concern, the prediction of its mechanical behavior has become an active field of research. Therefore, the improvement of bow modelling instruments has become essential.

Unfortunately, the lateral hydrodynamic force distribution inside the core is difficult to predict and requires large computational expense. Added to the fact that FA deformation is affected by multiple factors (structures and materials in the core, hydraulic forces, irradiation creep deformation, thermal gradients) makes this issue difficult to determine.

2. Objective of the Work

The consequences of bow in the reactor's safety and operating performance require an accurate prediction of the mechanical behavior of Fuel Assemblies towards deformation.

Many computational models [1,2,6] introduce numerical approaches based on the coupling of Computational Fluid Dynamics (CFD) and Finite Element Analysis (FEA) simulations, such as ANSYS CFX.

The objective of this thesis is the optimization of the model mesh which will best enable the most efficient, whilst still accurate, estimation of the lateral hydrodynamic forces inside the core. For this, it is necessary to reach convergence efficiently for different inlet profiles and structure deformation conditions of the Fuel Assemblies.

Since simulating the entire core's behavior with respect to bow would be too computationally expensive and time consuming due to the complex geometries of a PWR [1], it is necessary to make a compromise between accuracy of the results and computational cost. A porous model will be selected to simulate the hydraulics of an entire FA row.

The porous model contains certain "critical" regions, such as the gaps between Fuel Assemblies or the inlet and outlet regions of the spacer grids. Critical means, these regions behave differently towards deformation in comparison to the rest of the FA and, hence, gradients are relatively high compared. It will be, therefore, necessary to carry out a mesh optimization study in order to evaluate if the selected mesh does accurately simulate the behavior of these regions towards deformation.

The mentioned model is simulated for two different cases: Non-deformed and C-shape deformed FA structure. The aim of comparing the results from both cases is to determine whether the condition of structural deformation had an influence on the results of the study and on the convergence of the simulations.

Finally, a mesh independence study is carried out for both cases to determine which mesh provides mesh independent results, while accomplishing the requirements of accuracy and few computational expense.

3. The Pressurized Water Reactor

Pressurized Water Reactors constitute the large majority of all western nuclear power plants and are one of three types of Light Water Reactors (LWRs), the other types being Boling Water Reactors (BWRs) and Supercritical Water Reactors (SCWRs). PWRs, as the rest of LWRs, use water as both coolant and neutron moderator. PWRs are characterized by containing a pressurizer that maintains water at high pressure (about 15 MPa) in the primary coolant loop to prevent saturated boiling inside the core. The basic configuration of a PWR is shown in Figure 3.

The reactor consists of three main coolant loops:

The first one contains the reactor, where nuclear reaction takes place. A nucleus of enriched uranium undergoes fission, releasing thermal energy, which heats the water flowing through the reactor.

The produced thermal energy is then transmitted to the secondary loop, where the generated steam enters the turbine. This steam is then expanded producing mechanical energy, which drives a generator. Finally, electrical energy is obtained from the generator.

The third coolant loop contains the condenser. It is used to condense the exhaust steam coming from the turbine with water taken from an external source such as a river or the sea. To complete the cycle, the condensed water is pumped to the steam generator and the energy generation process starts again.

The main advantages of the Pressurized Water Reactors are:

- Robust and efficient reactor operations
- Highly stable reactors, as they produce less power when temperature increases
- The three loops are separated so that neither the turbine (secondary) nor the condenser (third) loops are contaminated by the radioactive materials contained in the primary loop.
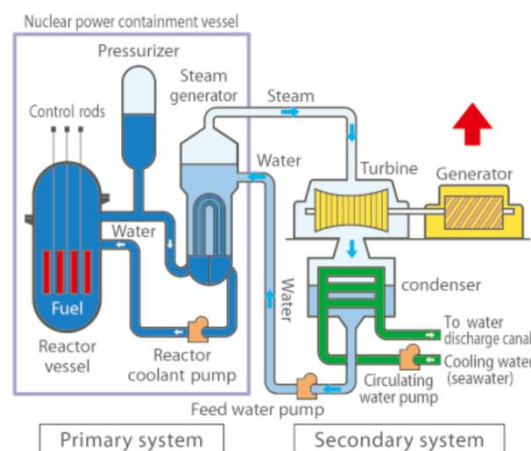
Figure 3: Basic configuration of a PWR [5]

3.1 Reactor pressure vessel

The reactor pressure vessel is a big cylindrical structure which contains the nuclear core and the mechanical support structures (Figure 4).The core is contained in a steel barrel with a surrounding reflector. Figure 5 shows the typical cross section of a PWR core. In the case of the PWR, the control rods are inserted from the vessel head. They are used to control the fission rate of uranium and plutonium inside the core, in other words, they are inserted in order to increase or decrease the neutron flux and hence the power output. In case of a sudden increase of power production, this offers a big advantage, because the control rods can be inserted by simple gravity.

The coolant enters the vessel through the coolant inlet nozzles and is distributed from the down-comer to the lower plenum, from there it enters the core from below. Then, the coolant travels up the core absorbing the produced thermal heat. Finally, the heated water is collected in the upper plenum and leaves the vessel through the outlet nozzles to the pressurizer.
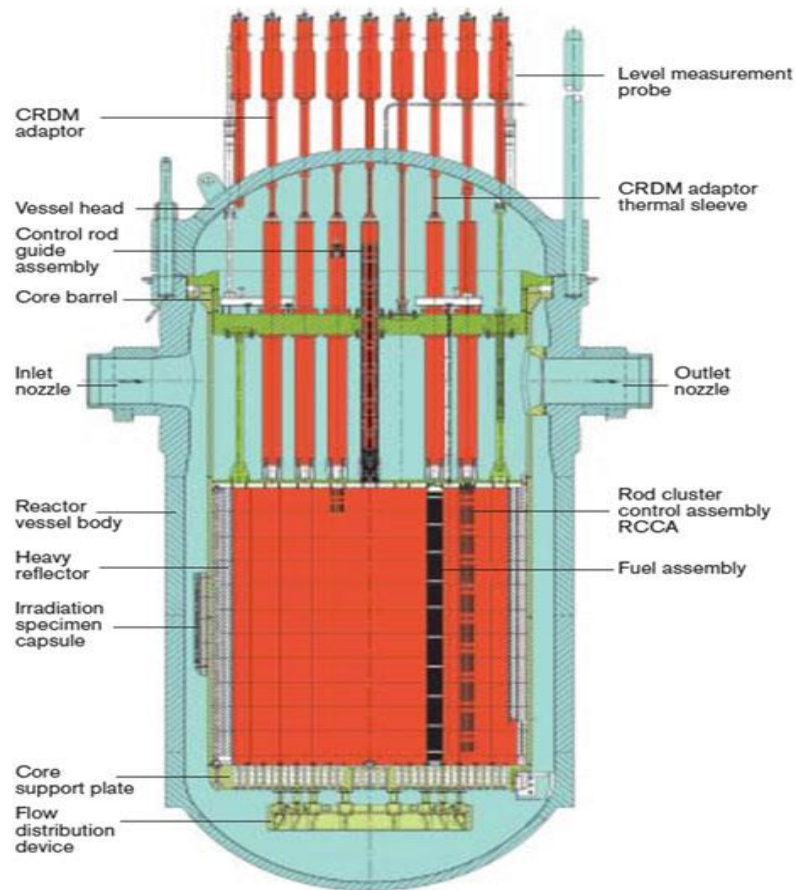
Figure 4: PWR reactor pressure vessel with core and internal components [6]
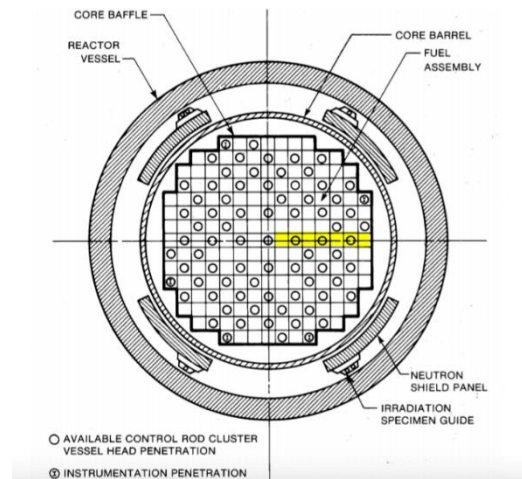
Figure 5: Cross section of a PWR core [5]

3.2 Pressurizer

The pressurizer (Figure 6) is a component of a PWR which regulates the pressure in the system (at about 15 MPa) in order to prevent the saturated boiling of the coolant. The pressurizer is basically a cylindrical pressure vessel, smaller than the reactor vessel and the steam generators.
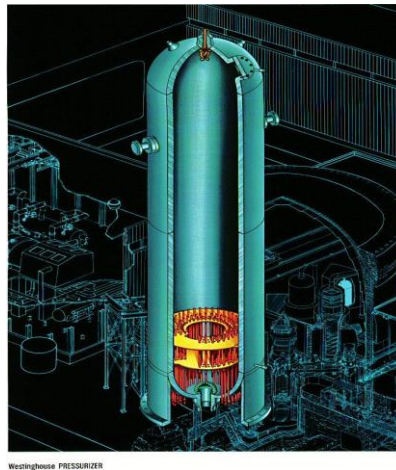
Figure 6: Pressurizer inside a PWR [5]

Pressure in the pressurizer is controlled by varying the temperature of the coolant in it. Large electric heaters in the pressurizer are switched on in order to increase the coolant temperature and thereby raise the pressure in the pressurizer. Pressure decrease is achieved by the use of sprays of relatively cool water inside the pressurizer, lowering the coolant temperature and therefore lowering the pressure. In case of excessive pressure in the pressurizer, a relief valve located on top of the pressurizer opens to avoid overpressure.

3.3 Steam generator

Steam Generators (SG) are heat exchangers used to convert water into steam from the heat produced in a nuclear reactor core. In PWRs, they are operating at about 7.6 MPa and   290 °C between the primary and secondary coolant loops. In commercial power plants, there are two to four steam generators per reactor. Figure 7 shows a U-tube steam generator, which is the most common SG used in nuclear power plants.
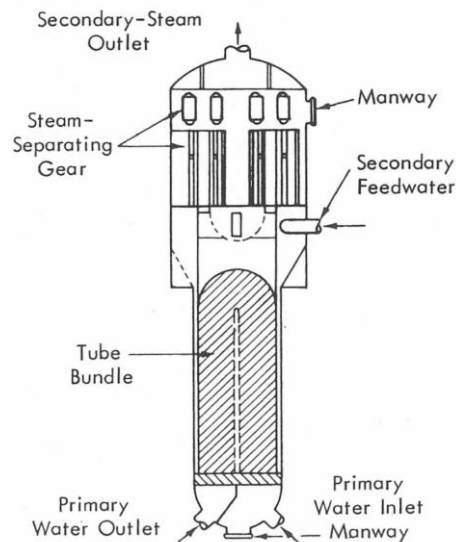
Figure 7: U-tube steam generator [5]

After being heated by the core, the coolant is then pumped through the primary tube side of the steam generator by coolant pumps. That water flowing boils and exits through the upper part of the SG. In order to prevent overpressure, a relief valve is placed at the top of the SG. Finally, the produced steam is delivered to the turbines to generate electricity.

3.4 Reactor coolant

From a nuclear point of view, coolants should have [7]:

- Low neutron absorption cross sections
- Low induced radioactivity
- Good radiation stability
- Strong moderating properties

From a Thermal-hydraulic point of view they should have

- High heat transfer coefficients to achieve higher power density.
- Low pumping losses requires low friction losses (low viscosity).
- Low cost: They must be economical

Liquid metals are the coolants with the highest heat transfer capability. Nevertheless, liquid metals are viscous and produce large pressure losses across the core.

Therefore, water is the most suitable reactor coolant for PWR operations margins.

3.5 Fuel Assembly

A Fuel Assembly is the array structure in form of squares that represents the fuel rods gathered into bundles. It contains top and bottom nozzle fastened to guide thimbles, for control rods and instrumentation. About 9 spacer grids are placed along the fuel rods, holding them in their position and acting as a kind of union. Together with the top and bottom nozzles, the aim of the grids is to provide structure and mechanical support to the Fuel Assembly.

As shown in Figure 8, the 4 meter long Fuel Assembly consists of 289 rods forming a square matrix (17 x 17 type). 264 rods contain fuel, while 24 are used for control rod guide thimbles. The one left is used for the instrumentation thimble.
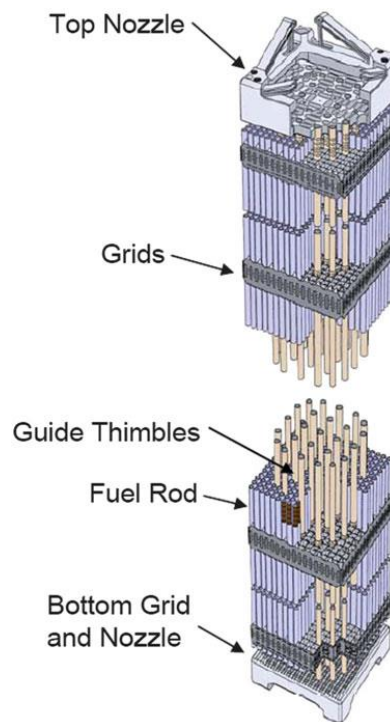
Figure 8: Fuel Assembly structure [6]

3.5.1 Fuel rods and spacer grids

Fuel rods are the elements which contain the nuclear fuel. For fission reactors, such as the PWRs, the fuel used is the enriched uranium dioxide powder (UO_2). The fuel is then pressed into ceramic pellets. The cylindrical pellets are surrounded by a zircaloy clad (Figure 9). zircaloy is chosen because of its mechanical properties and its low absorption cross section. The existing gap between the pellets and the cladding material is then filled with Helium to increase the heat gap conductance.

UO_2 has a very low thermal conductivity and uranium atom density in comparison to other materials, such as Mixed Oxide fuel (MOX). Nevertheless, UO_2 it is the most suitable fuel material because it has the largest chemical and irradiation tolerance by far.
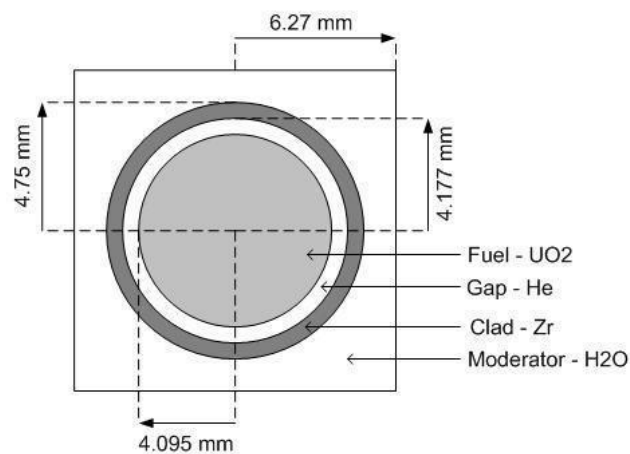
Figure 9: Cross section of a fuel rod and the zircaloy cladding [8]

Spacer grids hold fuel rods in their places to prevent them from vibrations (Figure 10). Their mixing vanes enhance cooling water mixing and heat transfer. It is here where the highest flow pressure losses happen creating an axial and lateral load on the structure.

Spacer grids provide structure and mechanical support to Fuel Assemblies, holding them in bundles and maintaining the lateral space between the rods. Together with the bottom and top nozzles and the guide thimbles, the grids constitute the skeleton of the Fuel Assembly, which is the main load-bearing structure maintaining integrity of the assembly. As they have a different geometry compared to the rods, high pressure gradients occur in the spacer grids inlet and outlet, leading to pressure form losses. According to [9], the structure of spacer grids enhances the mechanical strength, decreases hang-up susceptibility, and also influences thermal hydraulic performance, for example, pressure loss, mixing performance, and flow distribution.
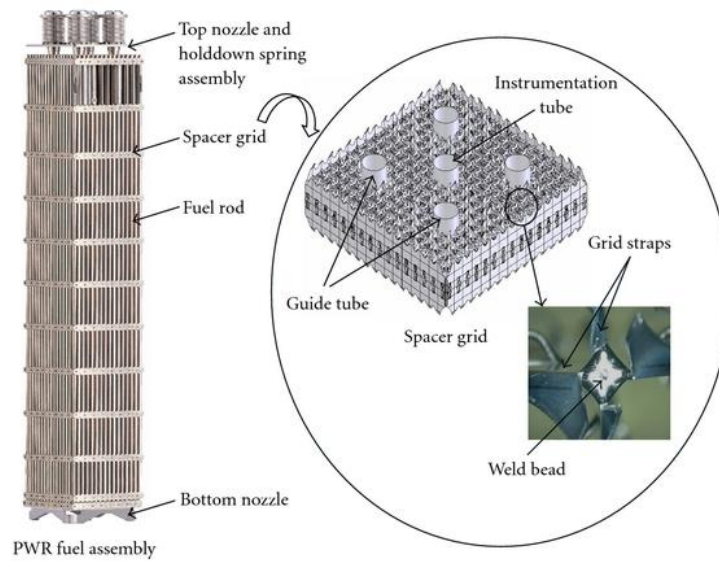
Figure 10: Fuel Assembly (left) and spacer grid (right) [10]

3.5.2 Control rods

The aim of the control rods in nuclear reactors is to maintain primary system temperature at the desired point by controlling fission chain reaction through the fuel fission rate. Control rods are similar to fuel rods, but containing high neutron absorption materials such as boron. In a PWR, they are inserted from the vessel head. Figure 11 shows the location of the control rods inside the Fuel Assembly. In case of a sudden increase of power production, this offers a big advantage, because the control rods can be inserted by simple gravity leading to a subcritical condition.
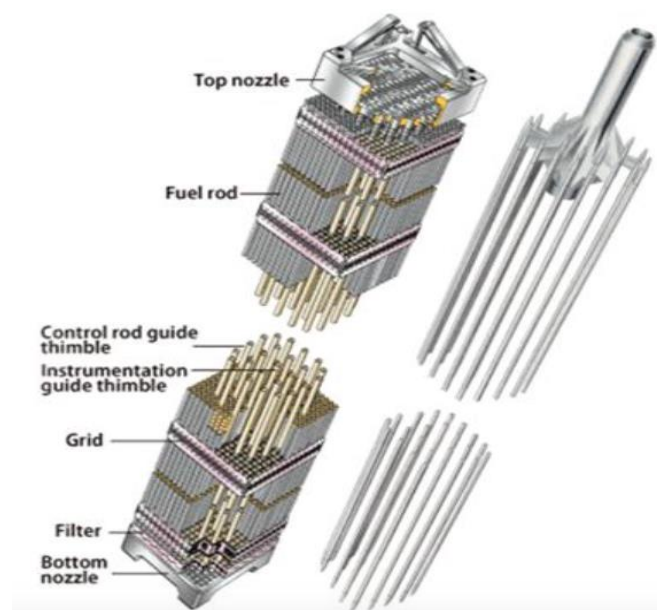
Figure 11: Control rod cluster inside a Fuel Assembly [8]

4 The Porous Model

A porous model is, by its definition, a medium of interconnected pores held together by a solid structure. A porous medium is characterized by its porosity factor, defined as the fraction of cross-sectional area occupied by the fluid compared to the total area of the Fuel Assembly.

$$\gamma = \frac{A_{FA} - A_{Rods}}{A_{FA}} \qquad (0\text{-}1)$$

The simulation of an exact PWR reactor core would be too computationally expensive. Instead, a porous model with a porosity of similar characteristics is constructed in order to make the simulation feasible. In this thesis, the porosity of the model equals to $\gamma = 0{,}556152$. This means, fluid moves across approximately 55% of the structure area, while the rest is comprised by the solid structure.

As stated in section 1, the existing pressure gradients inside the core are considered to be the main cause of the lateral hydraulic forces which lead to FA bow. These pressure gradients are generated by pressure drops in the reactor core. Therefore, it becomes essential to analyze the different pressure drops across the FA is order to predict its mechanical behaviour. The presented porous model is intended to estimate and simulate the mentioned forces and their impact on the FA structure.

4.1 Pressure losses

The main factors causing pressure drops in the core are described by the following equation:

$$\Delta p_{drop} = \Delta p_{friction\ rods} + \Delta p_{form\ grids} + \Delta p_{inlet/outlet} \qquad (0\text{-}2)$$

- The friction pressure drop in the fuel rod bundle: The contact between the clad walls and the coolant flow is the origin of this friction pressure drop.
- Form losses at the spacer grids: The presence of the spacer grids represents an obstacle for the flow, which derives in a form loss due to the change in the flow channel.
- Pressure losses at the core inlet and outlet: The core inlet and outlet present mainly pressure losses in axial direction. The lateral hydraulic forces are very low.

The resistance to flow of the presented porous medium will be accounted for by establishing appropriate pressure loss coefficients.

According to [11], there are four main pressure loss coefficients which have to be assessed:

- pressure loss coefficient in the rods in axial direction $K_{loss\ rods\ axial\ flow}$
- pressure loss coefficient in the rods in transversal direction $K_{loss\ rods\ crossflow}$
- pressure loss coefficient in the grids in axial direction $K_{loss\ grid\ axial\ flow}$
- pressure loss coefficient in the grids in transversal direction $K_{loss\ grid\ crossflow}$

A pressure loss does also exist along the gaps between two Fuel Assemblies, called the grid bypass. However, the pressure drop in it is very small compared to the mentioned pressure losses, and is therefore neglected.

4.1.1 Pressure losses in the rods in axial direction

The pressure losses caused by friction of the fluid with the solid walls of the rods is expressed as function of:

- Channel length L
- Hydraulic diameter D_h
- Velocity of the fluid v_{true}
- Average friction factor f

$$\Delta p_{friction} = f \frac{L}{D_h} \frac{\rho v_{true}^2}{2} \qquad (0\text{-}3)$$

Assuming turbulent flow inside the core ($Re > 10000$), the friction factor for axial flow is obtained as a function of the Reynolds number with McAdams equation.

$$f_{McAdams} = 0{,}184\ Re_{Axial}^{-0,2} \qquad (0\text{-}4)$$

As we are working with a porous model, the porosity modifies the velocity inside the channel:

$$v_{true} = \frac{v_{superficial}}{\gamma} \qquad (0\text{-}5)$$

True velocity is the physical velocity inside the domain and superficial velocity is the velocity before entering the porous domain.

The equations of the directional momentum losses are used in order to determine the pressure drop coefficients in porous regions. These equations presents a linear component, dependent on the viscous losses and a quadratic term representing the inertial losses.

$$S_{M,x} = \frac{K_{perm}}{\mu} U_x + \frac{K_{loss}\rho}{2} U_x{}^2 \tag{0-6}$$

$$S_{M,y} = \frac{K_{perm}}{\mu} U_y + \frac{K_{loss}\rho}{2} U_y{}^2$$

$$S_{M,z} = \frac{K_{perm}}{\mu} U_z + \frac{K_{loss}\rho}{2} U_z{}^2$$

Being U_x, U_y, U_z superficial velocities in x, y and z direction, respectively.

According to [8], viscous losses are neglected when using porous models based on turbulent pressure loss coefficients. Based on this assumption, the momentum losses will only take into account the quadratic term of the inertial losses.

The momentum loss in axial direction is equal to the derivative of the pressure drop along the rods:

$$S_{M,x} = \frac{\partial p}{\partial x} = \frac{f(Re)}{D_h} \frac{\rho v_{true}^2}{2} \tag{0-7}$$

As a result of coupling the las equations, the pressure drop coefficient in the rods in axial direction is determined:

$$K_{loss\,rods\,axial\,flow} = \frac{f_{McAdams}}{D_h\,\gamma^2} \tag{0-8}$$

4.1.2 Pressure losses in the rods in transversal direction

In order to evaluate the cross flow and the hydrodynamic forces in the reactor on Fuel Assemblies, a test called EOLE was developed [4]. This test aims to evaluate the pressure drop coefficient according to the Reynolds number and the slope angle between the flow and the rod bundle. These results enable us to establish an empirical correlation relating the pressure drop coefficient per rod row as a function of the slope angle θ, and the friction factor

$$K_{loss\,rods\,crossflow}(\theta) = \xi(\theta) * f_{crossflow} \tag{0-9}$$

Being the friction factor:

$$f_{crossflow} = aRe^b \tag{0-10}$$

For pure cross flow ($\theta = 90°$): a=1.85 and b= - 0.2

And $\xi(\theta)$ the Peybernes correction factor:

$$\xi(\theta) = \frac{\sin(\theta)}{\cos(\frac{90 - \theta}{2})}^{1.7} \qquad (0\text{-}11)$$

$\xi(\theta) = 0$ for pure axial flow ($\theta = 0°$) and $\xi(\theta) = 1$ for pure crossflow ($\theta = 90°$).   The   slope angle, also called angle of attack θ, is the angle of impact between the fluid and the rods. As FA bow occurs, the angle of attack varies. This means that, as the slope angle increases, the pressure drop coefficient in the transversal direction does also increase, reaching its maximum values for pure cross flow conditions.

Figure 12 depicts the deformed structure of a FA. The angle of attack is the sum of the structural rotation angle θ' due to bowing and the angle between the local flow direction and the former FA wall before being deformed θ_f.

$$\theta = \theta' + \theta_f \qquad (0\text{-}12)$$
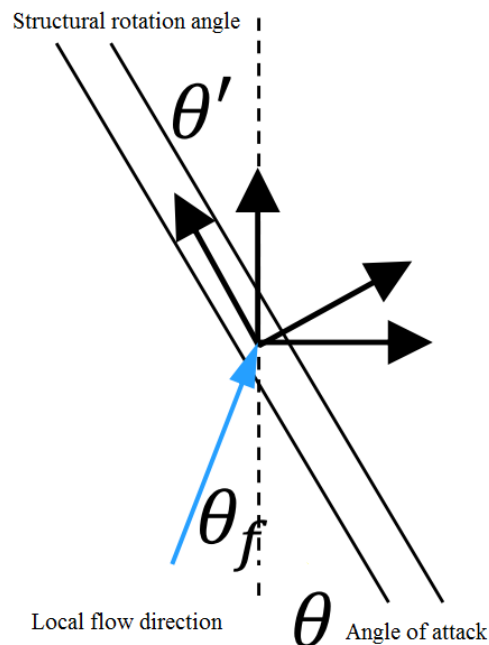
Figure 12: Angle of attack [11]

4.1.3 Pressure losses in the grids in axial direction

The pressure losses due to spacer grids or inlet or outlet geometry are classified as form losses. They correspond to a change in the coolant momentum due to a change in the coolant channel geometry.

$$\Delta p_{form} = \Delta p_{grids} + \Delta p_{inlet/outlet} = \sum_{i=1,...,loss} K_i \rho \frac{u_z^2}{2} \qquad (0\text{-}13)$$

K_i is a form friction factor due to a change in the coolant channel cross-sectional area. K_i has to be experimentally determined for each spacer grid design [7]. The pressure drop in axial direction inside the grids is determined by the following equation:

$$\Delta p_{grids\ axial} = K_{loss\ grid\ axial} \frac{\rho V_{sup}^2}{2} \frac{A_s}{A_v} \qquad (0\text{-}14)$$

Being A_s: Area occupied by the spacer and A_v= Flow Area of the rod bundle.

The pressure loss coefficient in the grids in axial direction is evaluated by [8]:

$$K_{loss\ grid\ axial} = \frac{K_{form\ grid} + K_{friction\ grid} + K_{rod\ friction}}{Grid\ Height} \qquad (0\text{-}15)$$

4.1.4 Pressure losses in the grids in transversal direction

Regarding the pressure loss coefficient across spacer grids due to cross flow, [11] assumed the lateral forces on the grid to be a reaction to changes of the fluids inertial force:

$$F_\perp = -m v_\perp \qquad (0\text{-}16)$$

The momentum loss in transversal direction is:

$$S_{M,\perp} = -K_\perp v_\perp \frac{\rho}{2} |v| = F_\perp m v_\perp = -\frac{\rho |v| v_\perp}{lgrid} \qquad (0\text{-}17)$$

Assuming:

$$S_{M,x} = \frac{\partial p}{\partial x} = \frac{\rho |v| v_{\perp}}{\text{lgrid}} = K_{\text{loss grid axial}} \frac{\rho V_{\text{sup}}^2}{2} \qquad (0\text{-}18)$$

The pressure loss coefficient in the spacer grids in transversal direction is determined:

$$K_{loss\ grid\ crossflow} = \frac{2}{l_{grid}} \qquad (0\text{-}19)$$

5. Modeling Approach: Computational Fluid Dynamics

Computational fluid dynamics (CFD) is an engineering method for simulating the behavior of systems, processes and equipment involving, among others, fluid flow problems.

More specifically, CFD can be coupled to structural mechanics to simulate its interaction with fluids.

In the field of nuclear energy, this tool becomes essential to analyze potential problems affecting the successful operation of nuclear power plants as well as its safety conditions.

In the recent years, research has focused, among other operating problems, on predicting FA bow, as it affected the performance and safety of nuclear power plants.

The use of CFD simulation is essential to predict the lateral flow distribution in the inner core which is the main cause for FA deformation[1, 5]. In this thesis, ANSYS ICEM CFD is used to create the geometry and the mesh of a FA porous model. The generated mesh is used by the fluid simulation tool ANSYS CFX to address the CFD inside the core providing safe and reliable solutions.

5.1 ANSYS ICEM CFD

ANSYS ICEM CFD is a mesh generation tool which offers the capability to parametrically create meshes from geometry. The meshes used to simulate the behavior of flow inside the reactor core are generated with this tool. Moreover, ICEM CFD is also a key element in mesh optimization. In this thesis, a mesh independence study is performed in order to assure that the obtained simulation results do not depend on the resolution of the generated mesh. This is further explained in section 7.2.

5.1.1 Geometry and blocking

First, the geometry of a FA is created. Its dimensions are depicted in Table 1:

Table 1: Geometrical dimensions of a Fuel Assembly

Element	Height X direction	Width Y direction	Depth Z direction
Fuel Assembly	4.5 m	0.2316 m	0.1 m
Rods	0.4965 m	0.2316 m	0.1 m
Spacer Grids	0.0485 m	0.2316 m	0.1 m

In the present model, the Fuel Assemblies are composed by two types of subdomains: the spacer grid region and the rod region. The Fuel Assembly consists of 10 fuel rod regions separated by 9 spacer grids. The rod dimensions described above are valid for the central rod spans. Note that the rods next to the top and bottom nozzles are shorter (Figure 13).
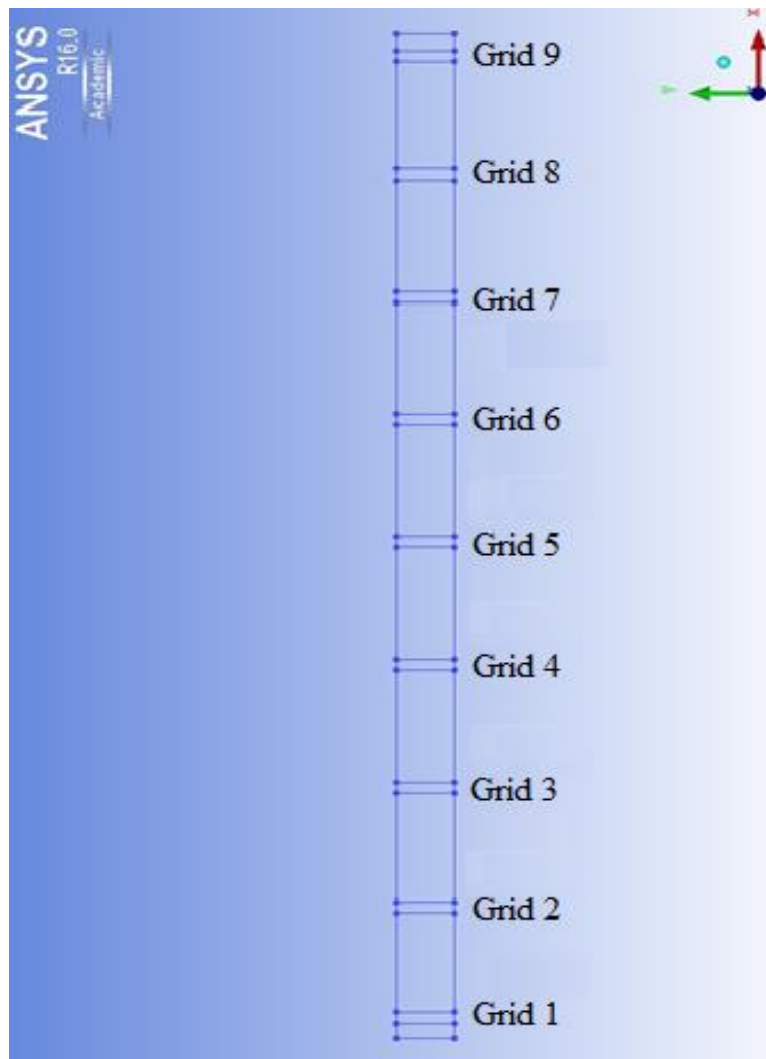
Figure 13: Geometry of a Fuel Assembly

Blocking is an essential step in mesh generation, since the structured mesh used to simulate the FA behavior towards bow is based on it.

The blocking strategy for the 2D Fuel Assembly geometry involves creating an initial block enclosing the whole geometry. The initial block is then split into 19 sub-blocks, which correspond to the 10 rod regions and 9 grids of the FA, and fitted to the geometry. This is achieved by creating associations between the edges of the blocks and the curves in the geometry and then, moving the vertices of the blocks onto the corners of the geometry.

Next, surface parts have to be created. A part is created for each external surface of the geometry. In case of the internal surfaces which are in contact with each other, (for example, RODS2DXPLUS 1 and GRIDS2DXMINUS 1), only one part is created, as this is in reality one single surface. The next step before mesh creation is associating each created part to its corresponding surface on the geometry (Figure 14).
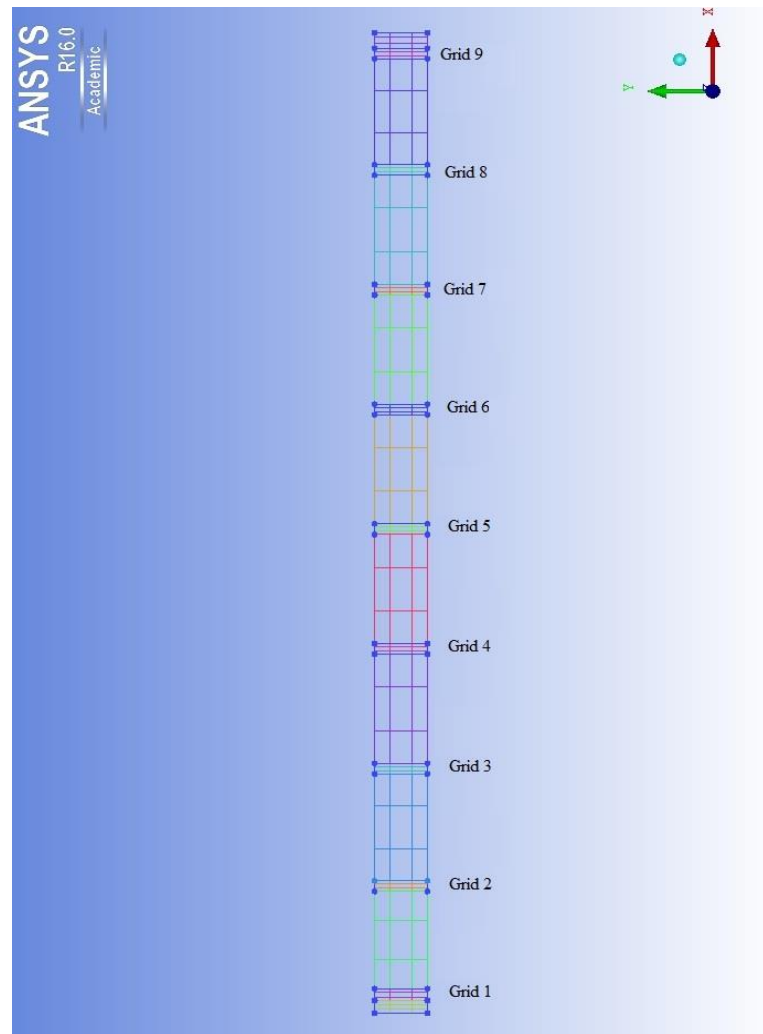
Figure 14: Parts associated to their corresponding surfaces in a FA

5.1.2 Mesh generation

Once the curve mesh parameters are defined, the initial mesh might be generated. Here, the main parameters that can be modified are:

- Number of nodes on the edges
- Node spacing size
- Ratio
- Mesh law

In this thesis, all lateral edges are supposed to have the same number of nodes to create a structured hexagonal mesh (Figure 15).
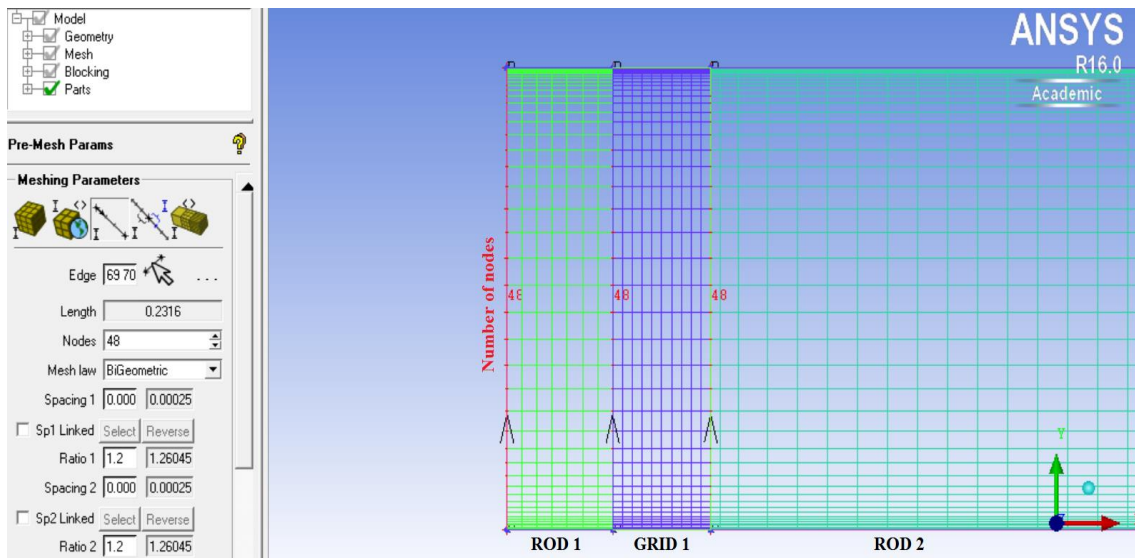
Figure 15: Number of nodes contained on the lateral edges of the mesh

In order to simulate a 2-Dimensional model, the number of nodes of all edges parallel to the Z-axis is set to 2, creating a domain with a depth of one single cell.

The amount of nodes on the axial edges depends on the position of the edge within the FA. As accurate numerical solutions are desired, meshes with fine spacing will be created in directions of most rapid local variation of solution variables and coarse spacing in other directions. Based on the geometry of this model, it is assumed that the core inlet and outlet, the transition regions between rods and grids, as well as the regions in contact with the gaps will present faster variation in their simulation output values. Regions where the solution varies rapidly are called "critical regions". In other words, edges close to the inlet and outlet (Figure 16) will have a higher density of nodes than edges within the domain (Figure 17). A deeper analysis of the meshing criteria in these regions is further explained in section 0.
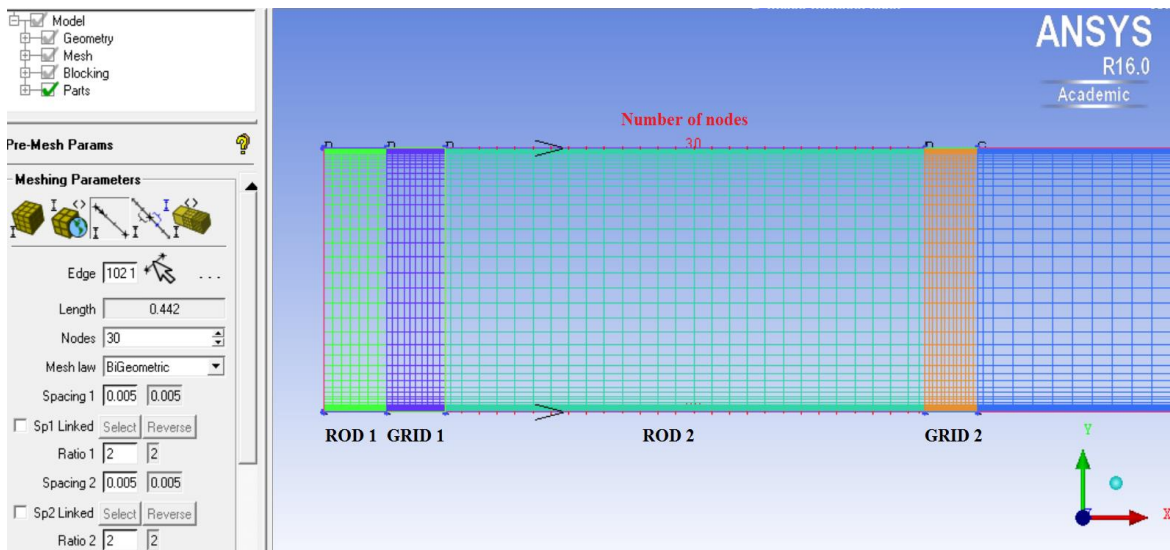
Figure 16: Number of nodes contained on the axial edges of a fuel rod close to the inlet
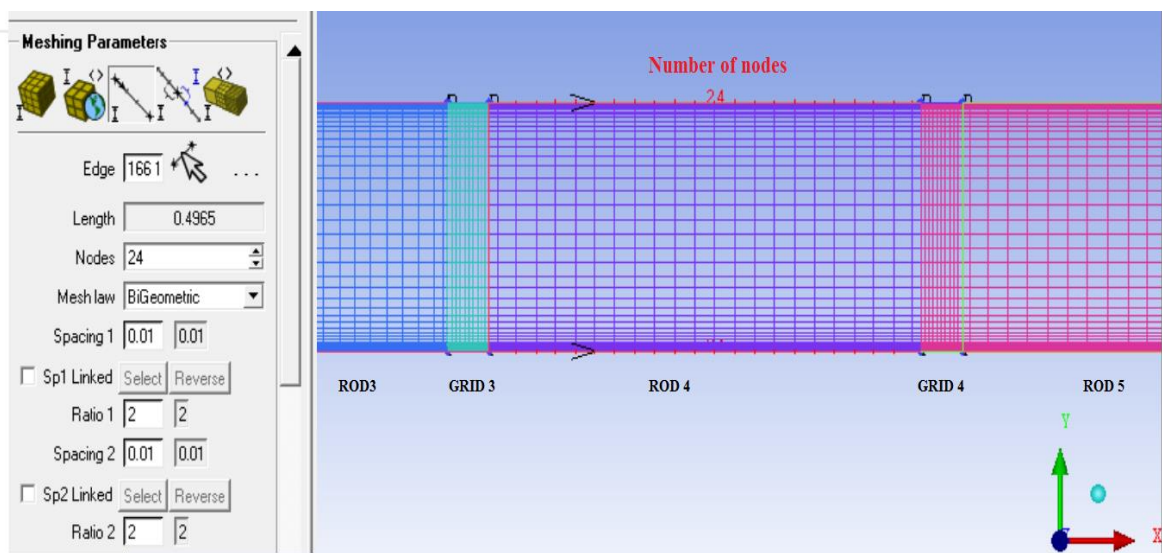
Figure 17: Number of nodes contained on the axial edges of a fuel rod within the domain

Parameter "spacing 1" refers to the node spacing size at the beginning of the edge, while "spacing 2" refers to the spacing at the end of the edge. A small spacing concentrates the grid points towards the beginning and end of the edge.

One of the mentioned "critical regions" is the area of the Fuel Assembly near the gaps. The node density was increased by introducing a small "spacing" parameter in the lateral edges in order to model their behavior towards deformation properly (Figure 18).
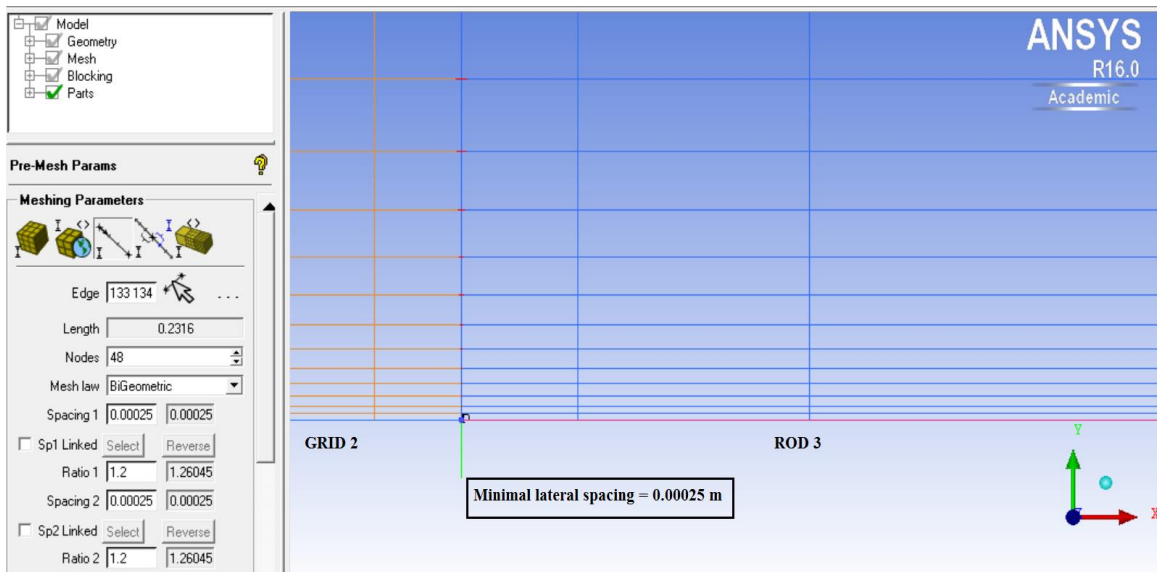
Figure 18: High concentration of nodes on the lateral edge boundaries of each FA

As mentioned in section 0 , the presence of the spacer grids represents an obstacle for the flow, causing a significant pressure drop due to the change in the flow channel. To obtain accurate results from simulation, this region will need a finer mesh, which is achieved by increasing the number of nodes in the axial edges in the transition area between fuel rods and spacer grids (Figure 19).
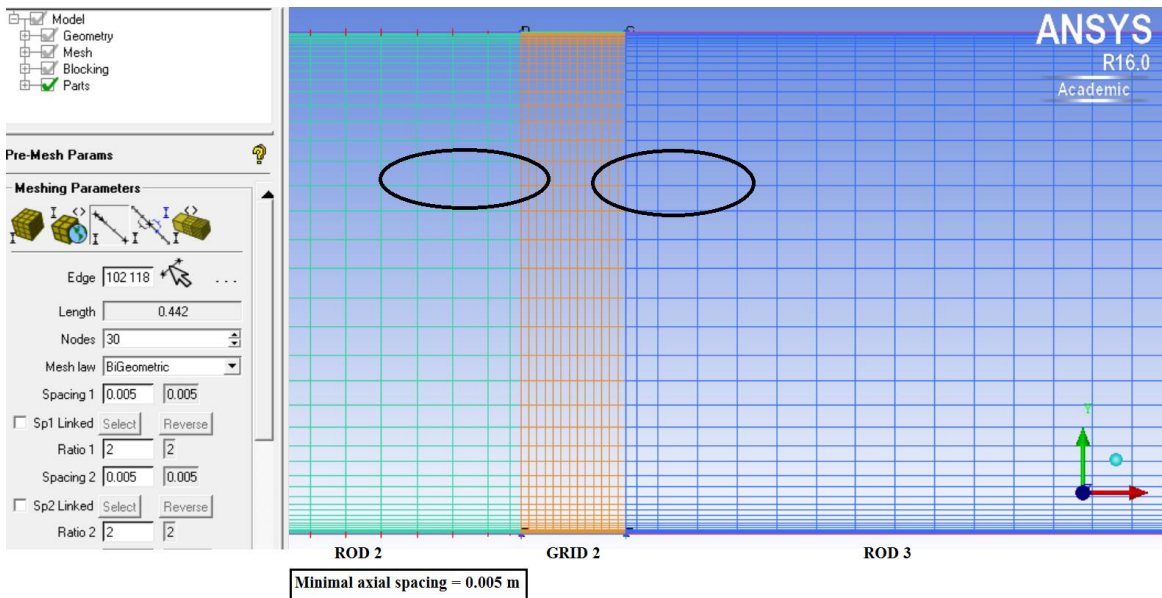
Figure 19: Small axial node spacing at the transition region between grids and rods

Note that the cell size in the rods (light and dark blue colored mesh) is much smaller in the region in contact with the grid than in the rest of the subdomain.

The parameter "ratio" defines the ratio in which the spacing between two adjacent nodes increases. This parameter is set automatically when the number of nodes and its spacing are defined. Finally, the mesh law is by default set to bi-geometric. This allows the nodes to be concentrated towards both ends of the edge.

Within this thesis, meshes with different amount of nodes are created in order to carry out a mesh independence study. The aim is to determine which mesh provides mesh independent results, while accomplishing the requirements of accuracy and few computational expense.

Table 2 represents the features of the created meshes, hence, mesh node density, lateral and axial node spacing and the refinement strategy followed to create them. Note that the mesh node density represents the number of nodes contained in each Fuel Assembly, not in the whole mesh.

The first mesh refinement strategy followed was increasing the cell density in a uniform manner within the domain (from 3472 to 14340 nodes). Then, the cell size was decreased especially in the "critical regions", so gap surroundings, core inlet and outlet and transition areas between fuel rods and spacer grids. The mesh refinement strategy was mainly focused on increasing the number of cells close to the gaps, considered to be the most critical regions, and was expanded by reducing the lateral node spacing. Mesh independence criteria are further discussed in section 7.2.

Table 2: Features and mesh refinement strategy of the created Fuel Assembly meshes

Mesh refinement strategy [Node number increase]	Mesh node density [Amount of nodes per FA]	Minimum lateral node spacing in the FA [m]	Minimum axial node spacing in the rods [m]
Uniform cell density increase	3472	0.002	0.03
	5406	0.002	0.03
Cell density increase in lateral edges and in the grids	9250	0.002	0.03
Uniform cell density increase	14340	0.0005	0.025
Cell density increase in lateral edges	16870	0.0005	0.025
Cell density increase in: Lateral edges Rods 2, 3, 8, 9 Grids 2, 8, 9	21140	0.00025	0.005
Uniform cell density increase	31488	0.00025	0.005

A representation of the mesh of the entire Fuel Assembly row can be found in the appendix (Figure 56).

5.2 ANSYS CFX

ANSYS CFX is a high-performance CFD software tool. It is commonly applied to accurately simulate fluid flow problems in a virtual environment. The set of equations solved by ANSYS CFX are the unsteady Navier-Stokes equations in their conservation form. CFX is recognized for its reliable results concerning the impact of fluid flows on the object of study.

It is divided in the following three modules:

5.2.1 ANSYS CFX Pre

CFX Pre is the preprocessing tool used by ANSYS. It is used to define the physical parameters required to describe the flow problem precisely. The most relevant tasks done in the preprocessing tool are: Importing the mesh and the physical expressions defining the behavior of the object of study, setting the boundary conditions and defining the material properties of the model. Files produced by CFX-Pre are sent to CFX-Solver.

5.2.2 ANSYS CFX Solver Manager

CFX-Solver Manager is a graphical user interface that iteratively solves the mathematical equations used to model fluid flow in ANSYS CFX and displays convergence history plots during problem solving. Convergence history plots show the behavior after each iteration of the Root Mean Square (RMS) residuals of the U, V, W components of momentum. The calculation stops when convergence is achieved. The convergence criteria and its assessment are further explained in section 6.1.

5.2.3 ANSYS CFD Post

CFX Post is a graphical post processing tool used to allow an easy and quantitative visualization of the CFX Solver results. It enables the visualization of the values of relevant parameters for the evaluation of the results along the object of study. Section 5.4 contains a deeper analysis of the results obtained after simulation.

5.3 ANSYS CFX Pre simulation setup

In this thesis, the simulation of the porous model is carried out for two different cases.

- Case 1: Simulation under conditions of no structural deformation
- Case 2: Simulation under C-shaped structural deformation

For both experiments, the same meshes, mathematical expressions and boundary conditions were used. The only exception was that the FA in case 2 was deformed in C-shape, that is, the gap positions were shifted according to the structural deformation (Figure 20).
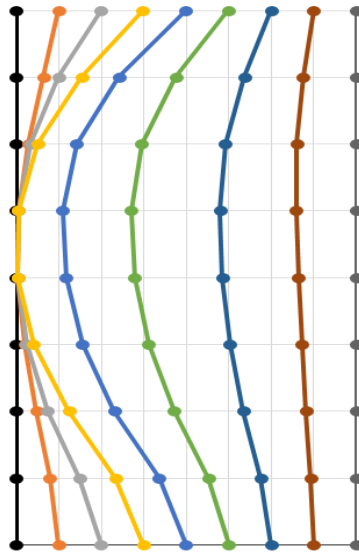
Figure 20: Representation of a C-shape deformed structure

The aim of comparing the results from both cases is to determine whether the condition of structural deformation had an influence on the results of the study and on the convergence of the simulations. A deeper analysis of the obtained simulation results is contained in section 7.1

5.3.1 Geometrical dimensions

The first step is importing the mesh of a single FA created in ANSYS ICEM CFD ("*SingleFA_DetailParts3.cfx5*"). This mesh is composed of different regions, called subdomains. In the present model, the Fuel Assemblies are composed by two types of subdomains: the spacer grid region and the rod region. Each Fuel Assembly (Figure 21) consists of 10 fuel rods (colored in red) separated by 9 spacer grids (colored in green). The geometrical dimensions of a Fuel Assembly are already listed in Table 1.
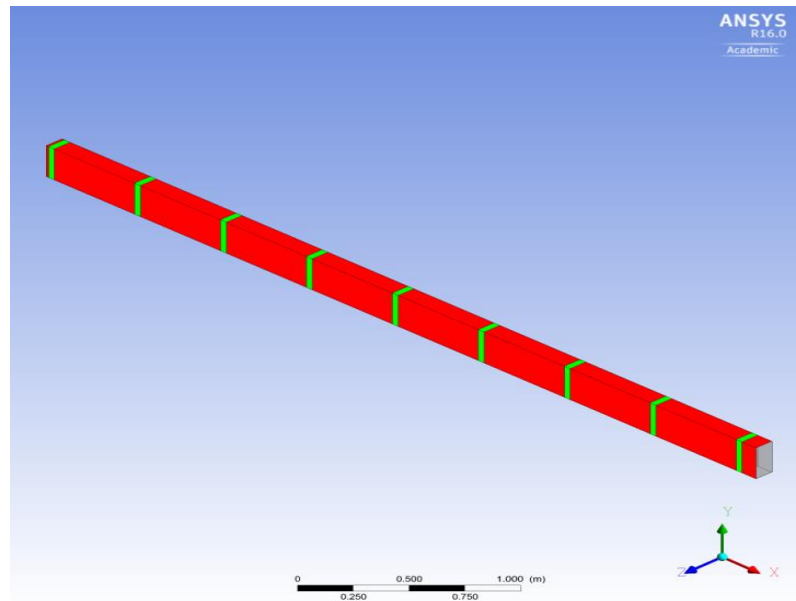
Figure 21: Representation of a single Fuel Assembly

The Fuel Assembly row is built up by playing the file "*MeshSetupWoGaps.pre*". This session file contains the mesh file created in ANSYS ICEM CFD, which is reproduced 7 times, as seen in Figure 22. Simulating the behavior of the entire core would be computationally too expensive, hence, only one single FA row is considered, which is assumed to consist of 16 FAs. To save simulation time, the present model size is further reduced by drawing a symmetry plane along [Y= 0.1158 m], where the 8 Fuel Assemblies are reflected to represent an entire PWR core row consisting of 16 FA. In reality, each FA is separated by a 2 mm nominal gap. The present model does not include geometrical gaps between the Fuel Assemblies, nevertheless they are included within the simulation. Section 0 includes further information about how they are modeled. The lower and upper core plate, as well as the bottom and top end pieces are not modelled, but the fuel rod bundle is elongated upstream the first, and downstream the ninth spacer grid.
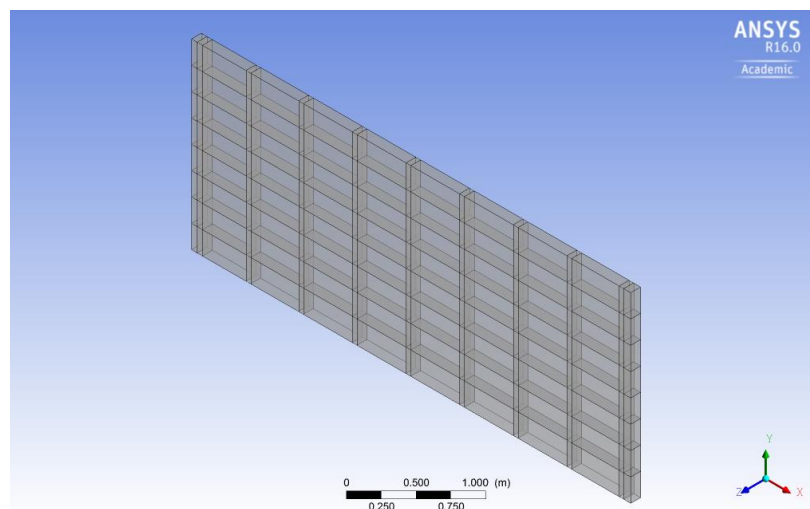
Figure 22: Representation of a Fuel Assembly row

5.3.2 Mathematical and boundary condition definition

Before running simulation, the mathematical expressions required for simulation are defined by the CFX Command Language (CCL) file "*ExpressionsFluid.ccl"*. The boundary conditions of the model are imported from the CCL file *"PreInputFile.ccl"*. Table 3 indicates the location of each boundary.

Table 3: Boundary condition definition

Element	Location
Core inlet	Plane X= 0.162 m
Core outlet	Plane X= 4.625 m
Core outer wall	Plane Y= -1.737 m
Center symmetry	Plane Y= 0.1158 m
Symmetry plane	Planes Z= 0.1 m and Z= 0.2 m

The coolant flow enters the Fuel Assemblies through the core inlet profile, which is depicted by the incoming black arrows (Figure 23). The outlet profile, indicated by exiting black arrows, is where the flow exits the domain.

A line of symmetry is drawn on the plane XZ to reflect the 8 FA and represent the entire core row. The outer wall, stands for the boundary between the core wall and the FA row. It is set as a smooth and no slip surface.

Finally, as the model is considered 2-Dimensional, the rear and frontal planes are also symmetrical boundary conditions.
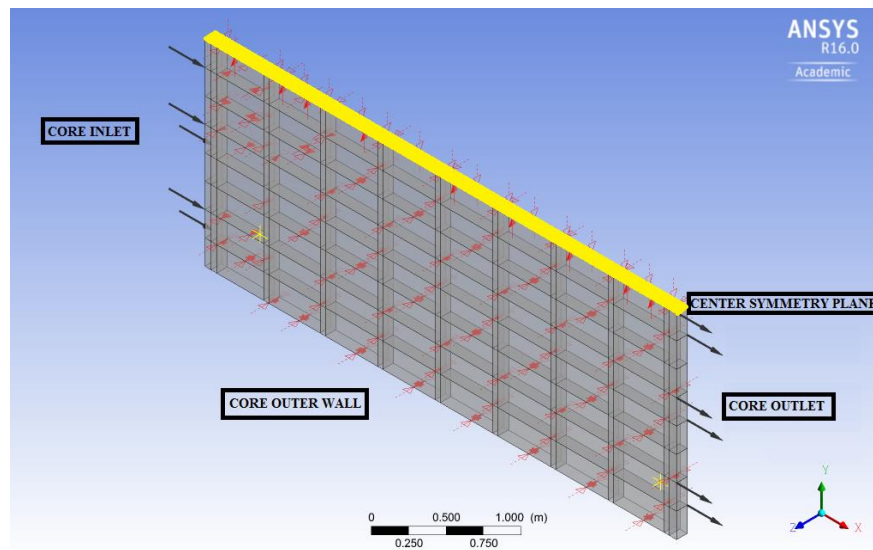
Figure 23: Boundary conditions in the FA row

5.3.3 Thermodynamic conditions

For the CFX Pre model, the following thermodynamic conditions are assumed:

- Reference pressure of 15.8 MPa (Similar to a real life PWR)
- Isothermal heat transfer
- Water is used as coolant fluid, at a reference temperature of 309 ºC
- The fluid turbulence follows the k-ε model

5.3.4 Velocity profiles

The following plots depict the assumed velocity profile in the core inlet and outlet boundary regions respectively. The represented range goes from the center of the FA row   [Y=0.1158 m] to the edge in contact with the outer core wall [Y= -1.737 m].

At the inlet and outlet boundary regions the following two boundary conditions were applied with respect to the coolant velocity profile:

- Increasing fourth-order polynomial velocity profile towards the FA center line
- Increasing fourth-order polynomial velocity profile towards the vessel wall

Vessel CFD studies were performed to determine flow patterns and turbulence inside Fuel Assemblies in PWRs [13] . The results indicate for the inlet region a higher mass flow rate in the center of the core than close to the periphery (Figure 24). The coolant velocity in the outlet, however, is higher in the region close to the FA row boundaries (Figure 25).
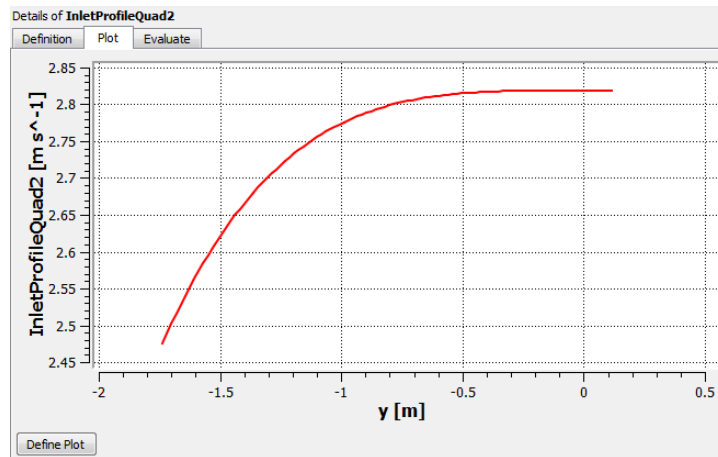
Figure 24: Coolant velocity profile at the core inlet region
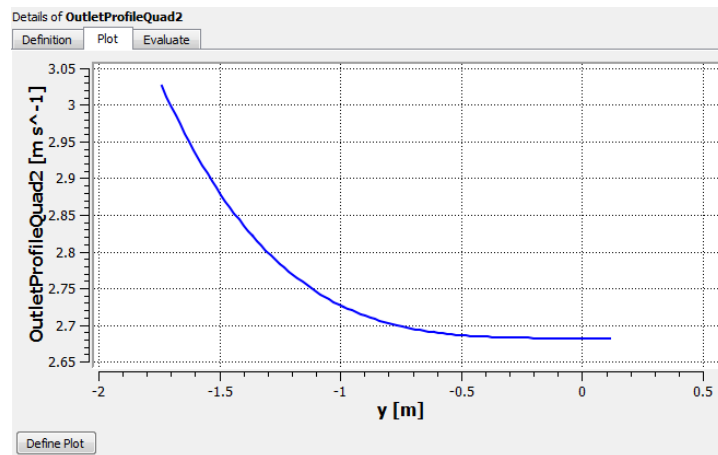
Figure 25: Coolant velocity profile at the core outlet region

5.3.5 Modifications in the gaps

In order to accurately simulate the real behavior of an operating PWR, the previous model used a separate subdomain for modeling the gaps with a different mesh with much higher cell density compared to the rest of the domain. This lead to convergence problems when running simulation.

The present new model includes the gaps within the fuel rods and spacer grids subdomain. For this purpose, a modified definition of the pressure drop within the gap region was necessary in order to obtain valid results from the simulation, as pressure drop coefficients are different in the gap region compared to the pressure losses inside the Fuel Assemblies.

This is simulated by implementing the pressure loss coefficients in the FA using a step function, which assumes a value of 0 within the gaps. With this variation, convergence problems were fixed.

5.3.6 Pressure drop coefficients in the rods region

To evaluate the pressure drop in the rods, the following average parameters of the coolant have to be determined:

- Density ρ
- Dynamic viscosity μ
- Superficial velocity in axial direction $v_{sup,axial}$
- Superficial velocity in transversal direction $v_{sup,crossflow}$

From literature [6], the following parameters are adopted for a standard 1300 MW-PWR, built by Kraftwerk Union in Germany (KWU-PWR):

- Coolant core inlet temperature: $T_{core\ inlet} = 292\ °C$
- Coolant core outlet temperature: $T_{core\ outlet} = 326\ °C$
- Coolant average pressure inside the core: $P_{average\ core} = 158\ bar$

Based on the mentioned values, the present model assumes the coolant flowing inside the core has an average temperature of:

$$T_{average\ core} = \frac{T_{core\ inlet} + T_{core\ outlet}}{2} = 309°C \qquad (0\text{-}20)$$

The average density of the coolant inside the core, expressed as a function of pressure and temperature, and its dynamic viscosity are obtained from steam tables:

$$\rho_{average\ core} = 707.7164029\ \frac{kg}{m^3}$$

$$\mu_{average\ coolant} = 8.85 * 10^{-5}\ Pa\ s$$

The model assumes a mass flux inside the sub-channel of $G_f = 3500\ \frac{kg}{s\ m^2}$.

According to [7], the mass flux is:

$$G_f = \rho_{average\ core\ coolant} * v_{true,axial} \qquad (0\text{-}21)$$

Since the simulation is based on a porous model ($\gamma_{core} = 0.556152$), the superficial velocity of the fluid in axial direction is calculated from equation (5-2).

$$v_{sup,axial} = 2.7529524\ \frac{m}{s}$$

Consequently, Figure 26 and Figure 27 represent the value of the pressure loss coefficient in the rods in axial and lateral direction for the range [Y= - 0.56 m; Y= - 0.58 m], respectively. It is

important to note, that this region represents the transitions between the third and the fourth FA, including the gap between them.

The values of the pressure drop coefficients in the rods are:

- $K_{loss\,rods\,axial\,flow} = 3.18374 \text{m}^{-1}$ inside the Fuel Assembly.
- $K_{loss\,rods\,crossflow} = 23.7235 \text{ m}^{-1}$ inside the Fuel Assembly.
- $K_{loss\,rods\,axial\,flow} = K_{loss\,rods\,crossflow} = 0 \, m^{-1}$ in the gap.
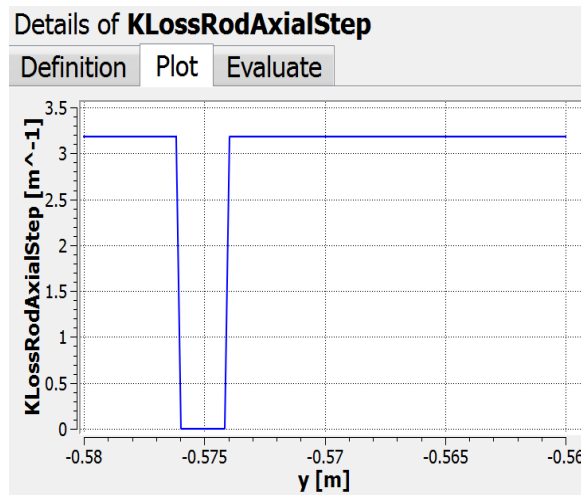
Figure 26: Pressure drop coefficient in the rods in axial direction
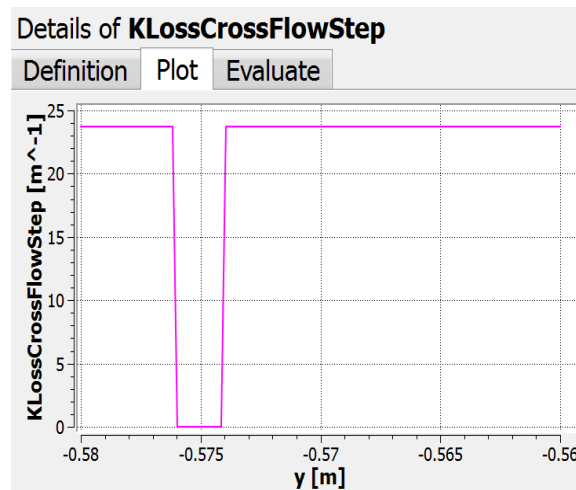
Figure 27: Pressure drop coefficient in the rods in transversal direction

5.3.7 Pressure drop coefficients in the grids

Consequently, Figure 28 and Figure 29 represent the value of the pressure loss coefficient in the rods in lateral and axial direction for the same range [Y= - 0.56 m; Y= - 0.58 m].

The values of the pressure drop coefficients in the rods are

- $K_{loss\ grid\ crossflow} = 452.176\ m^{-1}$ inside the Fuel Assembly.
- $K_{loss\ grid\ axial\ flow} = 44.8715 m^{-1}$ inside the Fuel Assembly.
- $K_{loss\ grid\ crossflow} = K_{loss\ grid\ axial\ flow} = 0\ m^{-1}$ in the gap.
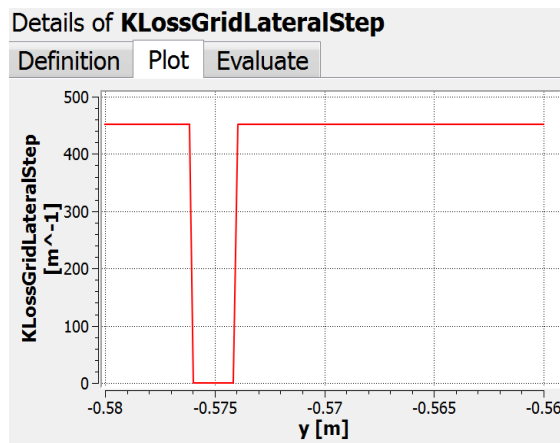
Figure 28: Pressure drop coefficient in the grids in transversal direction
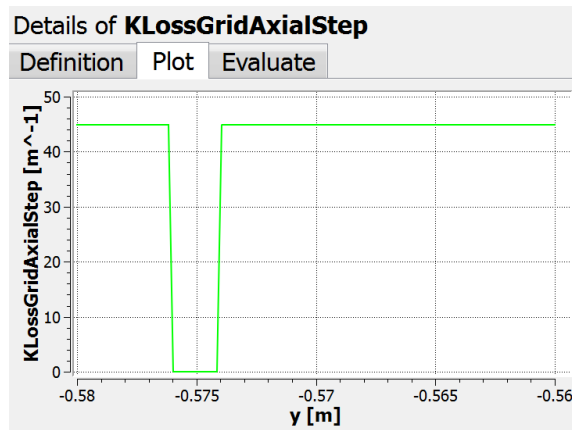
Figure 29: Pressure drop coefficient in the grids in axial direction

5.4 CFD Post: Visualization of the obtained results

The analyzed results are obtained from the simulation with the mesh containing 14340 nodes for the non-deformed and the C-shape deformed structure.

The aim of visualizing the simulation results is two folded:

First, comparing the results from both cases allows us to determine whether the condition of structural deformation had an influence on the results of the study and on the convergence of the simulations.

Second, determining the magnitude and distribution of the crossflow coolant velocity inside the core is essential in order to evaluate in which regions solution variables change rapidly within the present model, thus needing a finer mesh.

Figure 30 depicts an entire FA row. Within this model, the FA next to the reactor wall   [Y= -1.737 m] is considered the first FA and the eighth FA the one in contact with the center line of the row [Y= 0.1158 m]. As mentioned in Table 3, the core inlet and outlet are located at [X= 0.162 m] and [X=4.625 m], respectively.
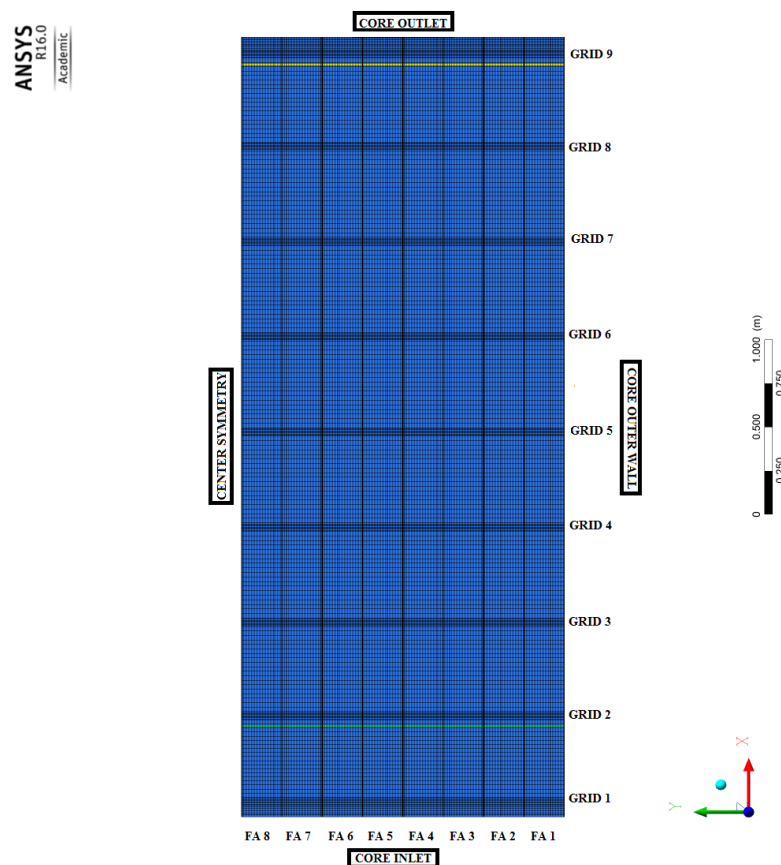
Figure 30: Representation of an entire Fuel Assembly row

The domain regions close to the core inlet and outlet are assumed to be "critical". To prove this assumption, the coolant velocity profile in transversal direction is represented in   Figure 31. The fastest solution variables changes take place in the first and ninth spacer grid, thus confirming the mentioned hypothesis.
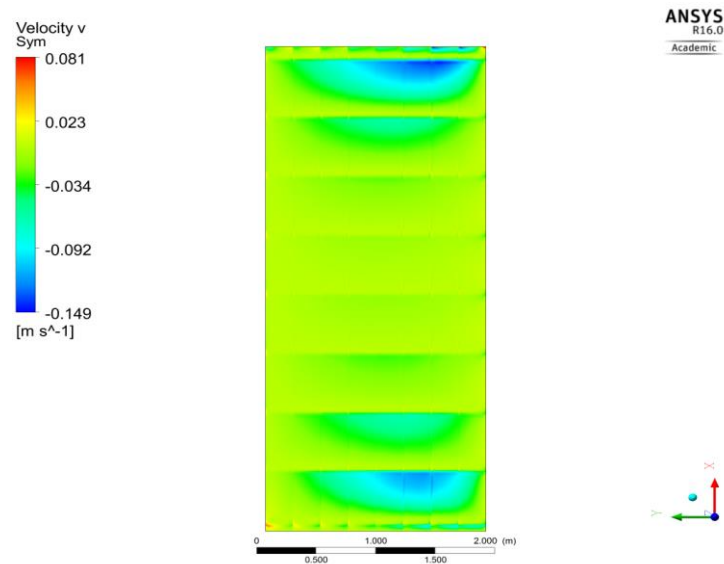
Figure 31: Non-deformed structure: Lateral velocity profile inside the core

A closer look on the lateral velocity along the transversal direction is required. The green and the black line represented in Figure 30 are located at the axial levels [X= 0.683 m] and [X= 4.47 m], respectively. They indicate the regions with the highest values for the lateral velocity. Figure 32 compares the values of the lateral velocity along the mentioned lines.
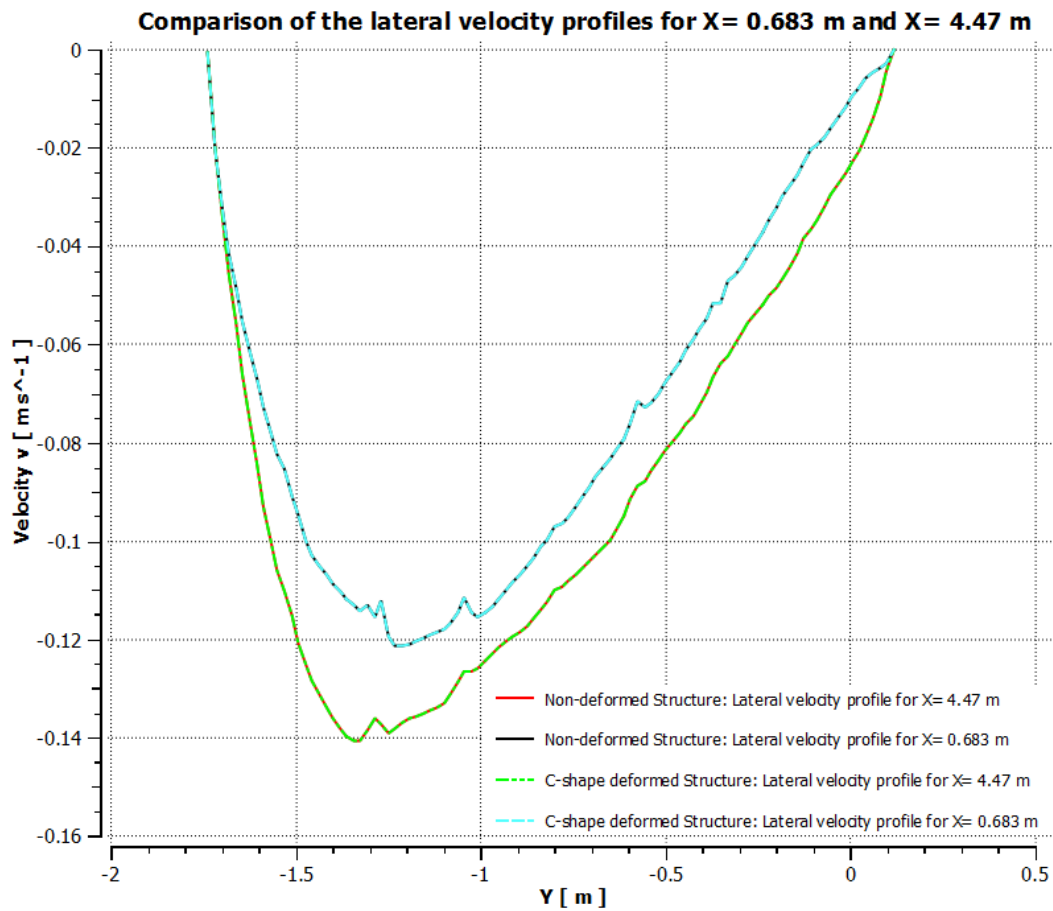
Figure 32: Comparison of the lateral velocity profiles at [X= 0.683 m] and [X= 4.47 m]

The peak value for the transversal velocity is achieved at [Y= -1.34 m], which corresponds to the transition region between the second and third FA. Figure 33 plots the lateral velocity at this region along the axial direction.

The lateral velocity value drops in the transition region between rods and spacer grids. This is due to the high lateral flow resistance of the grids which derive in form pressure losses. These rapid changes in the lateral coolant velocity values indicate the need for a mesh refinement concerning the transition regions between fuel rods and spacer grids.
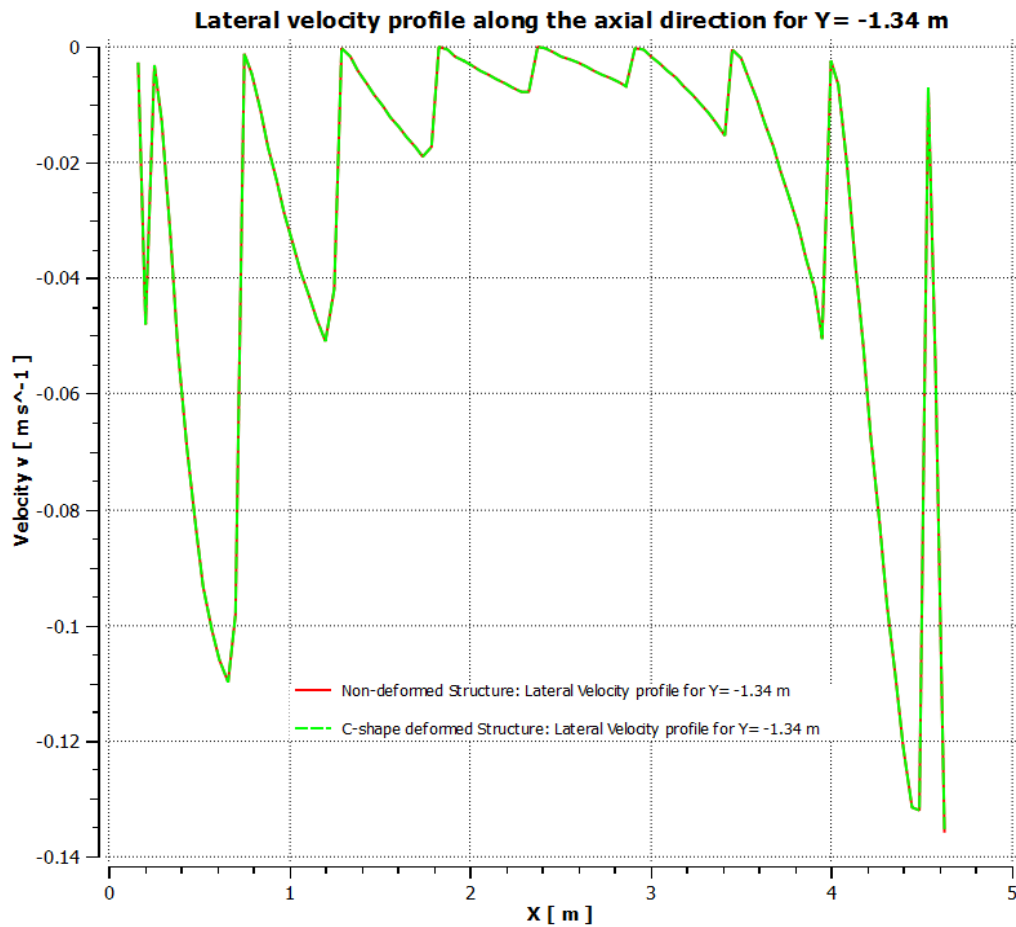
Figure 33: Lateral velocity profile along the axial direction at [Y= -1.34 m]

Figure 34 plots the axial velocity profile at the axial level [X= 0.683 m] along the transversal direction in order to analyze the influence of the gaps between the Fuel Assemblies on the simulated model. Generally, the axial flow velocity remains stable throughout the whole FA row, except for the gap region. The fact, that the pressure loss coefficient is assumed to be 0 within the gaps results in a much higher mass flow rate within this region (up to 8.53% more in the gap between the sixth and the seventh FA). The abrupt variation of the axial velocity varies in the gap regions supports the assumption, that the gap regions are "critical" and need a finer mesh if accurate results are desired.
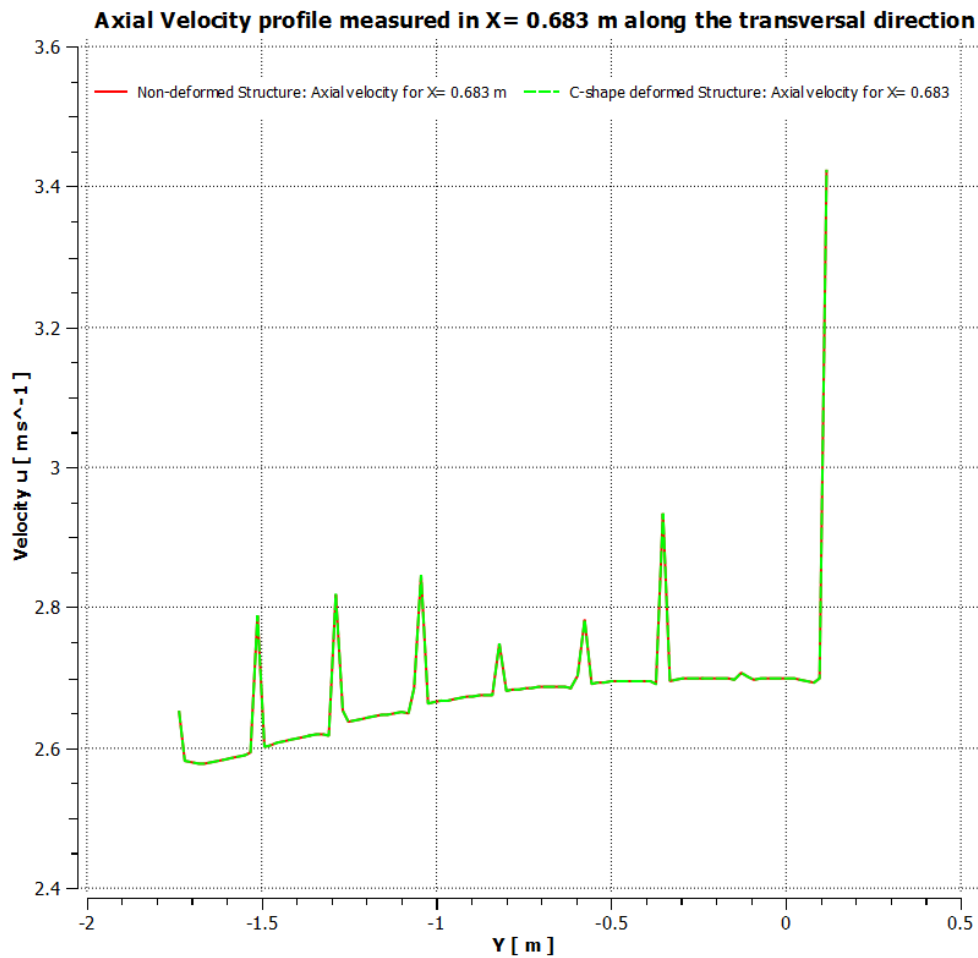
Figure 34: Axial velocity profile measured at [X= 0.683 m] along the transversal direction

Figure 35 represents the pressure distribution inside the core. At the core inlet, the pressure is high, and diminishes progressively towards the outlet. Initially, the system's reference pressure was set to 15.8 MPa, which corresponds to the average pressure in the pressure vessel. Therefore, some results have negative pressures based on the reference pressure.

Figure 36 depicts the pressure gradient in axial direction inside the core. The pressure gradient of the coolant inside the core requires further analysis, as it is considered one of the main causes of the hydrodynamic forces which have a fundamental role in FA bowing.
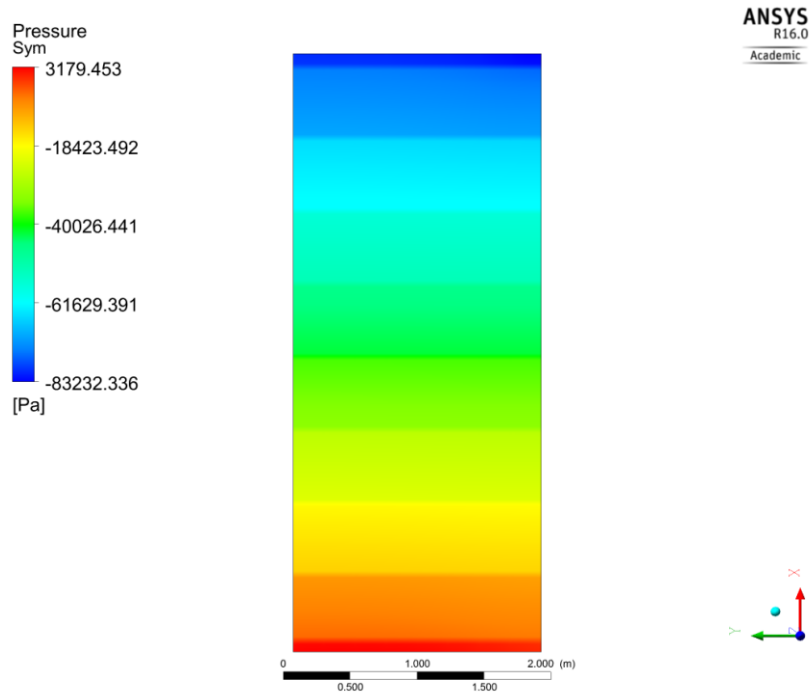
Figure 35: Pressure distribution inside the core
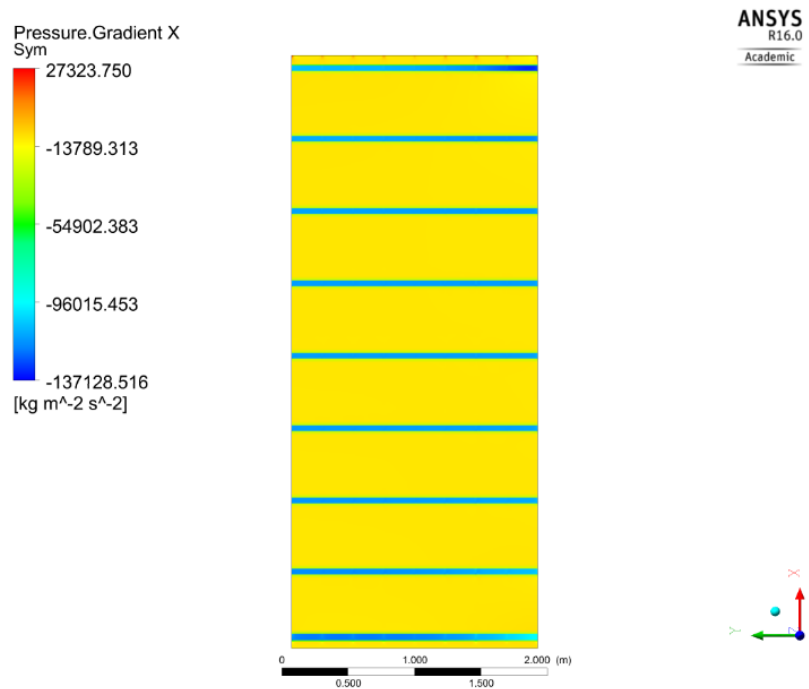
Figure 36: Pressure gradient of the coolant in axial direction inside the core

The high pressure drops present in the spacer grids call for a deeper analysis. Figure 37 displays the pressure gradient along the axial direction in the center of the FA row at   [Y= 0.1158 m]. The pressure drop is stable along the FA, but increases abruptly in the spacer grid regions, mainly due to the form pressure losses. The presence of the grids represents an obstacle for the flow, which derives in a form loss due to the change in the flow channel. This confirms again the assumption that the solution variables present rapid variation in the transition regions between the rods and the grids and consequently need a finer mesh.
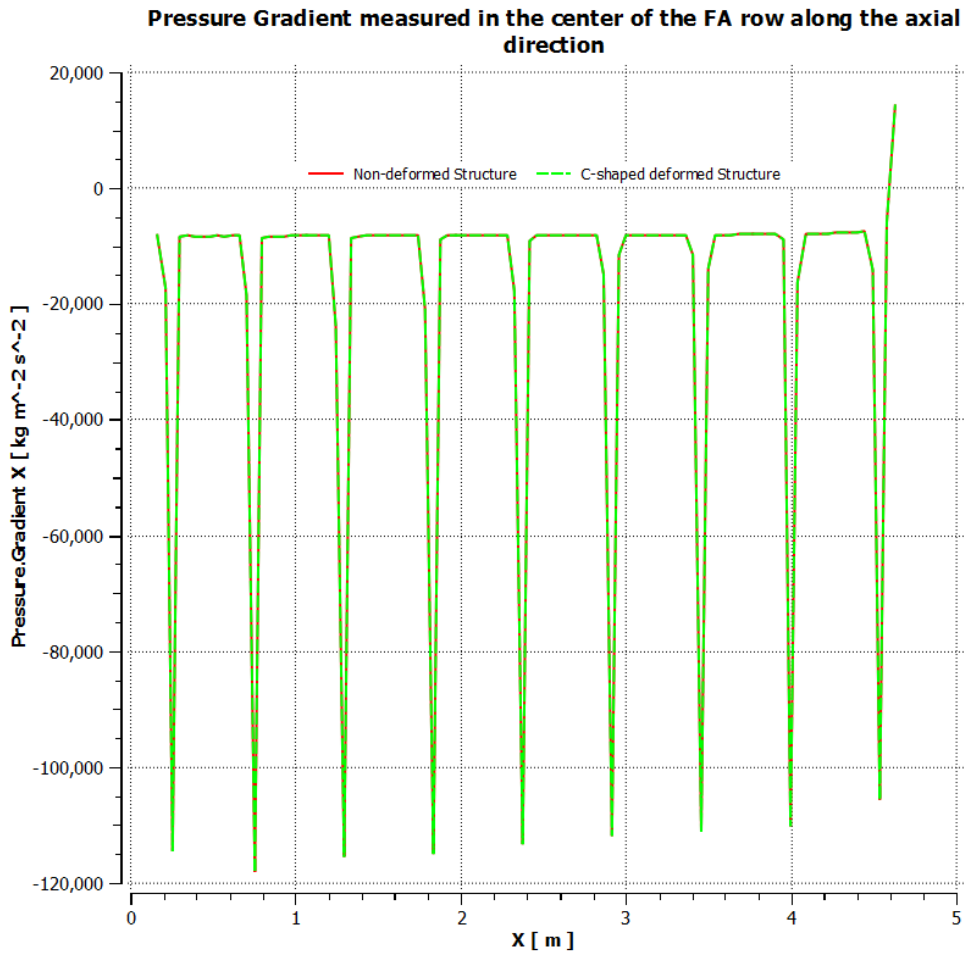
Figure 37: Pressure Gradient measured in the center of the FA row along the axial direction

6. Accuracy and reliability assessment in computer simulation

Scientific research of physical processes has used computer simulation to assess accuracy and reliability of the engineering systems. The credibility of the computational results is of great concern due to the impact, mainly on performance and safety aspects, that modeling and simulation predictions can have on engineering. Therefore, it is essential to critically evaluate confidence in modeling and simulation results. According to [14], verification and validation of computational simulations are the primary methods for building and quantifying the confidence in simulation results.

The definition of verification given by [15] is:

Verification: "The process of determining that a model implementation accurately represents the developer's conceptual description of the model and the solution to the model".

The fundamental strategy of verification is the identification and quantification of errors in the computational model and its solution. In verification activities, the accuracy of the obtained results is generally measured in relation to highly accurate solutions of simplified model problems.

In other words, verification provides evidence that the conceptual model is solved correctly by the mathematics contained in computer simulation. Figure 38 depicts the verification process of comparing the numerical solution with various types of highly accurate solutions.
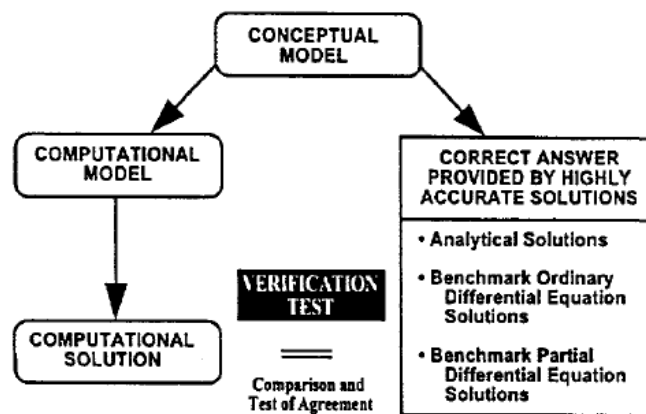
Figure 38: Verification process [15]

On the other hand, validation is defined as "the process of determining the degree to which a model is an adequate representation of the real world from the perspective of the intended usage of the model".

The accuracy is measured by experimental data, which is the best measure of reality. Figure 39 depicts the validation process of comparing the computational results of the modeling and simulation process with various types of experimental data.
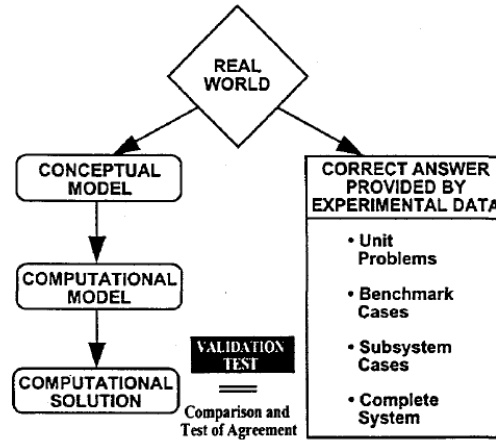
Figure 39: Validation process [15]

The fundamental strategy for validation is to:

- Identify and quantify the error and uncertainty in the conceptual and computational models.
- Estimate the experimental uncertainty and compare it to the computational results.
- Quantify the numerical error in the computational solution.

To identify computational errors, it is necessary to previously define which kind of errors exist. From reviewed literature, computational errors can be split into two types of errors: Acknowledged or unknown errors [15].

Unknown errors are usually mistakes, for example in the definition of the boundary conditions. There are no methods for estimating these kinds of errors.

On the other hand, acknowledged errors are characterized by an approach that is considered to be more accurate, for example approximations made to simplify the modeling of a physical process, and conversion of PDEs into discrete equations used in CFD. These errors are called discretization errors, and can be measured by a careful convergence assessment.

Solution convergence is fundamentally asymptotic. From this perspective, the only real confidence we can have in a calculation is, if sufficient discretization resolution is achieved to directly confirm solution convergence.

In conclusion, validation of computational fluid dynamics requires significant evidence that the equations of the underlying conceptual model are solved accurately. Solution convergence implies giving stability and consistency to the results. In simpler words, validation requires solution convergence.

6.1 Convergence assessment

6.1.1 The importance of convergence

The solution process of fluid flow problems is an iterative process in which values are changing from one iteration to the next. Significant changes in the results mean the results upon which our decisions are based are also changing significantly. Therefore, there is a need to define when a solution is complete, in other words, when the iterative process converges to a certain value.

6.1.2 Convergence conditions

There is no strict rule to judge when an analysis has converged. Therefore, analysts should have a solid understanding of when the analysis has reached its final solution, since they do define the point at which the solution is converged.

Generally, steady state simulations need to ensure that the final solution satisfies the following conditions to consider a valid solution:

- Residual RMS Error values have been reduced to an acceptable value.
- Solution imbalances are less than 1%.
- Monitor points for the defined values of interest have reached a steady solution.

The Root Mean Square (RMS) residual value is one of the most fundamental measures of an iterative solution's convergence, as it directly quantifies the error in the solution of the system of equations. Since CFD calculations are iterative, the residual will never be exactly zero. However, the lower the residual value is, the more numerically accurate the solution.

In this thesis, RMS residual levels of 10^{-4} are considered to be loosely converged, levels of 10^{-5} are considered to be well converged, and levels of 10^{-6} are considered to be tightly converged.

Residuals are not a direct measure of solution accuracy. They are a measure of the numerical imbalance of the Partial Differential Equations (PDEs). Therefore, another measure of convergence is checking the global imbalances of the PDEs. As a numerical representation of a physical system, the CFD solution imbalances will never be exactly zero. However, the imbalances should be less than 1% before considering the solution as converged.

A necessary condition is the convergence of the defined values of interest to a steady solution. Values of interest are essentially the main outputs from the simulation: pressure drop, forces, velocity or mass flow.

In the present model, monitoring points are placed to track the value of the lateral velocity at the locations where the value it reaches is relatively high (Table 4). Lateral velocity is directly related to the lateral forces, which are the main cause of FA deformation. Ensuring that these physical quantities have reached a steady solution confirms that the decisions are based on a single repeatable value, thus considering the obtained solution valid.

Table 4: Coordinates of the lateral velocity monitoring points

	Cartesian coordinates in [m] [X]	Cartesian coordinates in [m] [Y]	Cartesian coordinates in [m] [Z]
Monitoring Point 1	0.683	-1.214	0.2
Monitoring point 2	4.4737	-1.34	0.2

6.1.3 Factors affecting a converged solution

A converged solution means that the best solution for the given problem has been achieved. However, this does not imply that the solution is in accordance to real conditions. There are other factors involved which can influence the accuracy of the results, such as:

- Boundary definition
- Discretization errors

If flow features do not seem reasonable, the boundary conditions should be checked, as they have a great influence on the results. An accurate definition of the boundary conditions ensures that the obtained solution is the numerical solution for the previously defined problem. The more accurate the boundary conditions, the more accurate the converged solution will be.

There are often differences between the exact analytical solution of the modeled differential equations and the converged solution of their discrete representations. These differences are referred to as discretization errors.

A useful procedure for reducing the level of discretization error existing in a CFD solution is the grid convergence study, also known as mesh independence study. Grid convergence is necessary to achieve accurate numerical solutions.

It consists in progressively approaching the zero discretization error as the number of grid cells increases and the size of the grid spacing tends to zero. As the mesh is refined, the solution should become less sensitive to the grid spacing and the discretization errors should vanish. A poor quality or coarse mesh will thus induce errors in the final solution.

Specifically, the most effective strategy for accomplishing this is to reduce mesh spacing in regions of rapid solution variation. As a globally fine mesh is not realistic due to its computational expense, the error is reduced by generating meshes with fine spacing in directions of most rapid solution variation and coarse spacing in other directions. This procedure is further explained in section 0.

7. Results

7.1 Convergence Analysis

ANSYS CFX solver manager is used in this thesis to determine the convergence of the simulations to a steady solution.

The ANSYS CFX Solver Manager is an interface that is generally used to view the relevant data during problem solving. CFX Solver solves iteratively the continuity equation (P-Mass) and the momentum equations in axial and transversal direction (U and V, respectively). Since a 2D model is simulated, the momentum equation in W-direction is neglected. The RMS residuals are plotted at the end of each iteration time step for the P-Mass equation and the U, and V components of momentum.

7.1.1 Convergence based on RMS residuals

At the beginning, convergence problems appeared when running simulation. The main cause was, the mesh in the gaps was too fine and couldn't simulate its behavior properly. As mentioned in section 0, step functions were created where the pressure loss coefficients had a value of 0 in the gaps. With this variation, convergence problems were fixed.

The amount of iterations needed before convergence depends on how well the mesh adapts to the model and is able to solve its PDEs. A finer mesh may better represent the underlying physics of a problem, thus yielding faster convergence. But also the opposite is possible. A coarser mesh may also stabilize the solution process by smearing out numerically unstable regions.

In the present case, convergence is reached first by the fine meshes, (Figure 42 and Figure 43) then by the coarse meshes (Figure 41 and Figure 40). It is achieved simultaneously for the non-deformed (Figure 40 and Figure 43) and the C-shape deformed structure (Figure 41 and Figure 42), confirming structural deformation has no influence on the simulation's convergence.

As seen in the plots, all RMS residual levels decrease after 27 iterations in case of the fine meshes and 35 iterations, in case of the coarse meshes, below 1E-4. At this point, solution is considered to be converged.
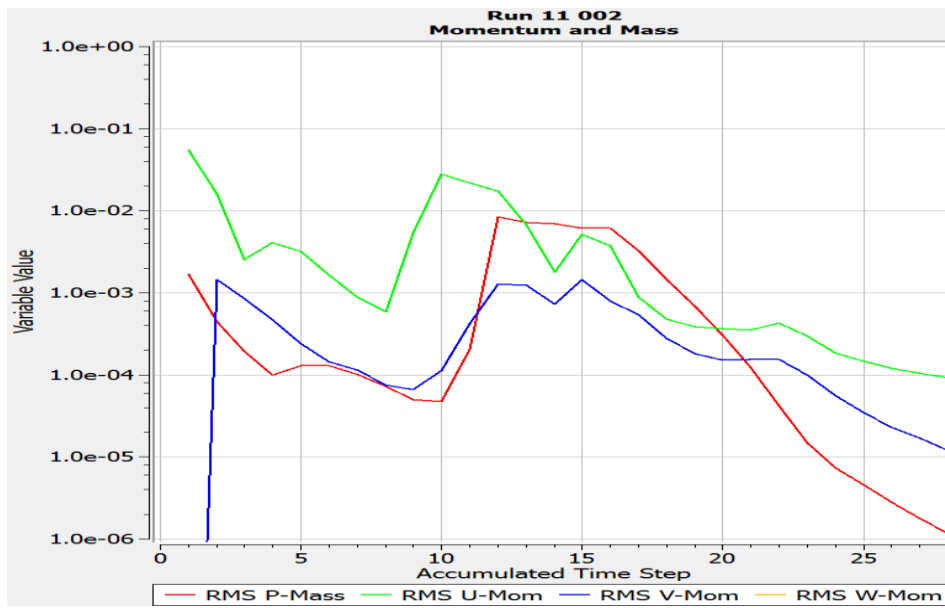
Figure 40: Convergence of the Residual RMS values for the non-deformed structure simulations containing 3472 nodes
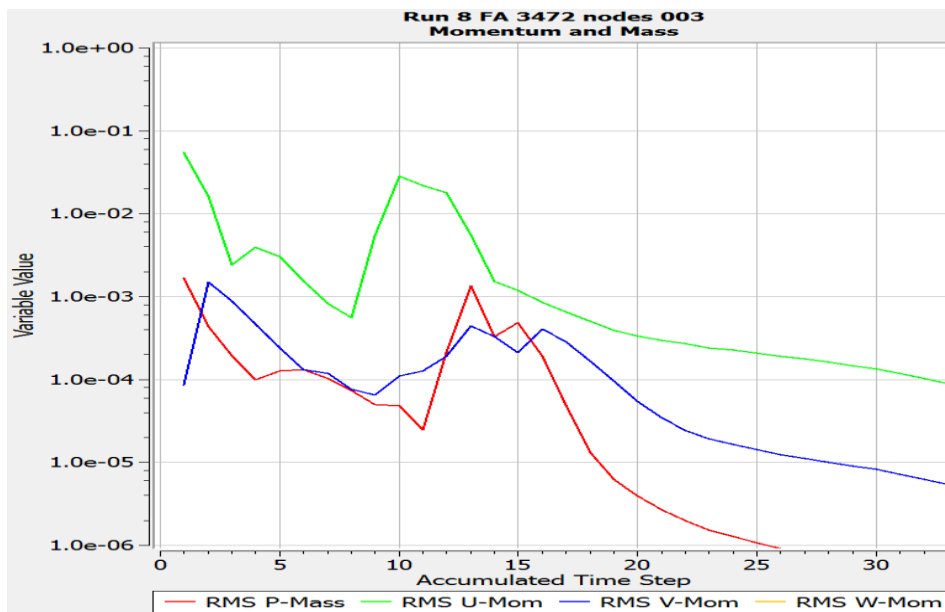
Figure 41: Convergence of the residual RMS values of the C-shaped mesh simulation containing 3472 nodes
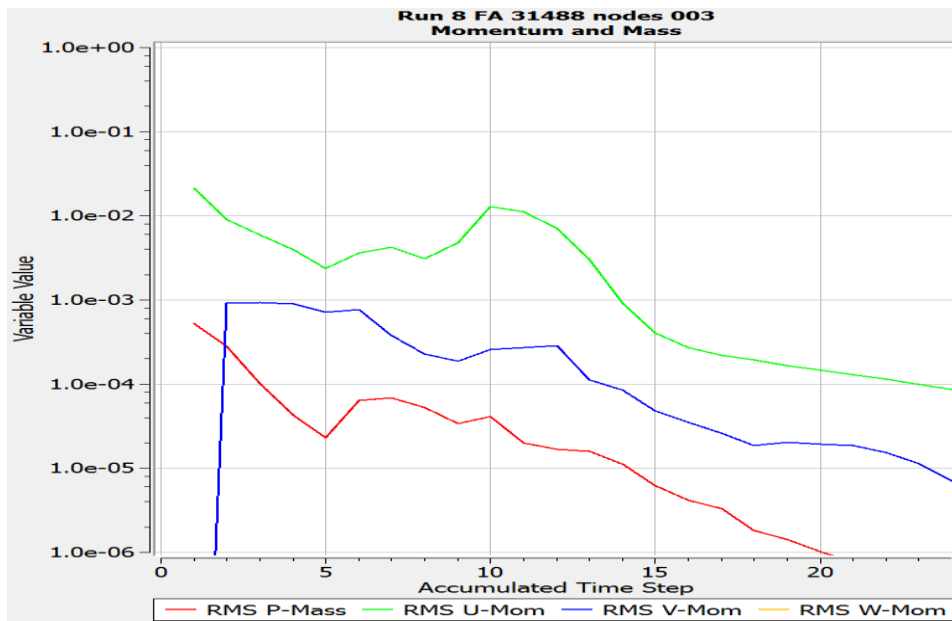
Figure 42: Convergence of the residual RMS values of the non-deformed mesh simulation containing 31488 nodes

12.54
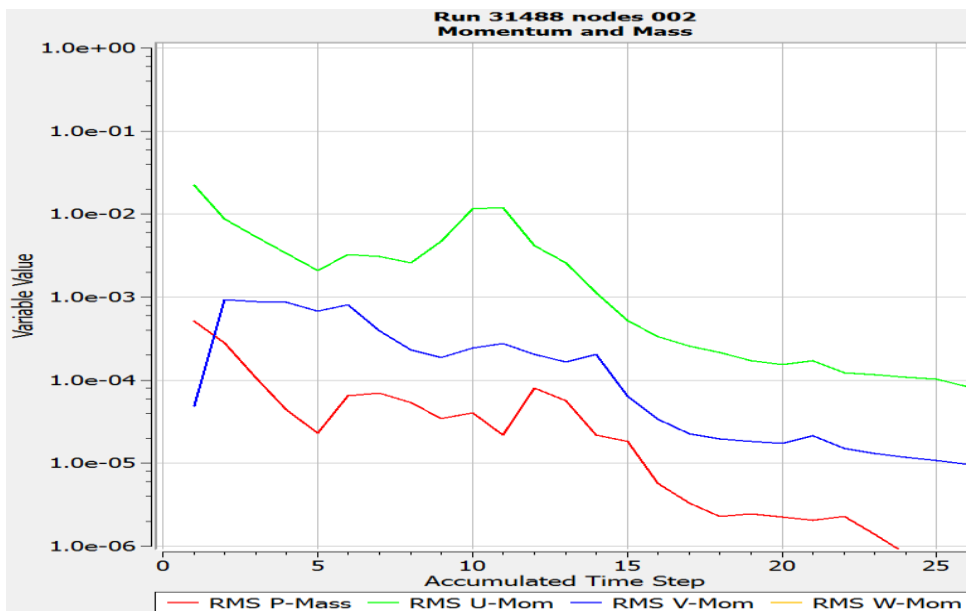
Figure 43: Convergence of the residual RMS values of the C-shaped mesh simulation containing 31488 nodes

7.1.2 Convergence of the monitoring point values

As mentioned in section 0, steady state simulations do not only need to reduce their residual RMS value to an acceptable value. Another necessary condition is the convergence of the defined values of interest to a steady solution. Values of interest are essentially the main outputs from simulation.

In the present model, monitoring points are placed to track the value of the lateral velocity at the locations where the value it reaches is relatively high (Table 4). Lateral coolant flow velocity is directly related to the lateral forces, which are the main cause of FA deformation. Ensuring that these physical quantities have reached a steady solution confirms that the decisions are based on a single repeatable value, thus considering the obtained solution valid.

Figure 44, Figure 45, Figure 46 and Figure 47 plot the value of the lateral velocity in the monitor points against the number of iterations.

After approximately 10 iterations, the tracked values have flattened out, thus confirming also the convergence of the transversal velocity at the monitoring point's location.

It is also demonstrated that structural deformation has no impact on the convergence of the lateral velocity values.
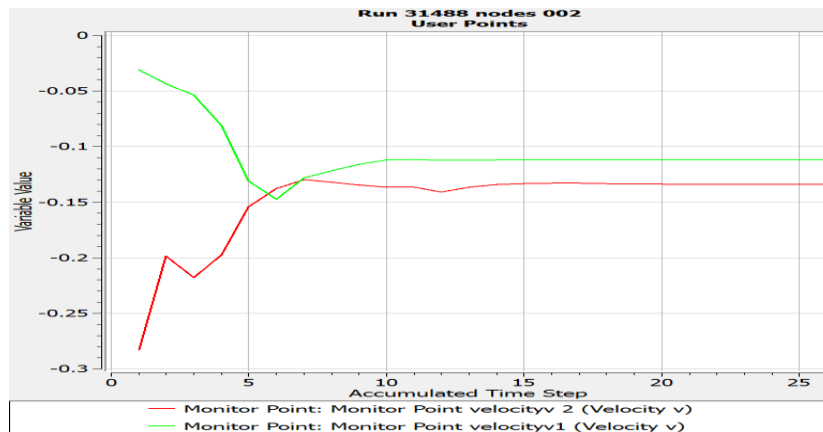
Figure 44: Convergence of the lateral velocity for the C-shaped mesh simulation containing 31488 nodes
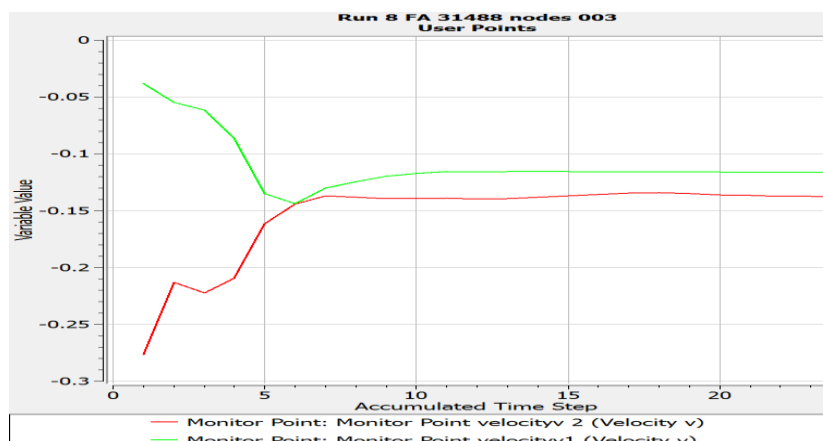
Figure 45: Convergence of the lateral velocity for the non-deformed mesh simulation containing 31488 nodes
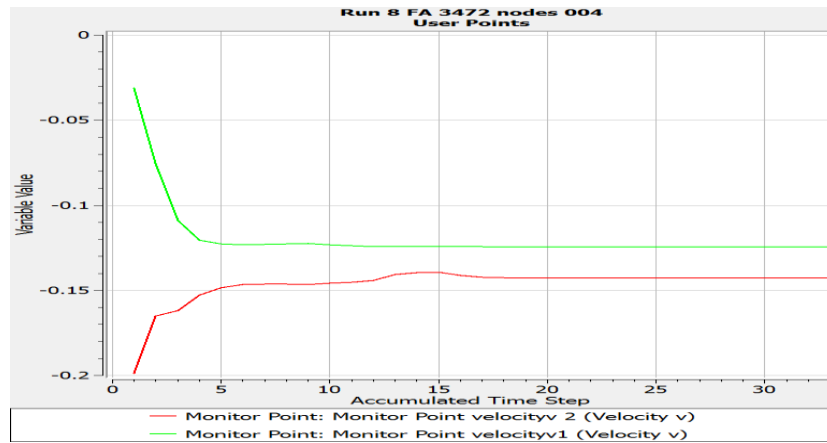
Figure 46: Convergence of the lateral velocity for the C-shaped mesh simulation containing 3472 nodes
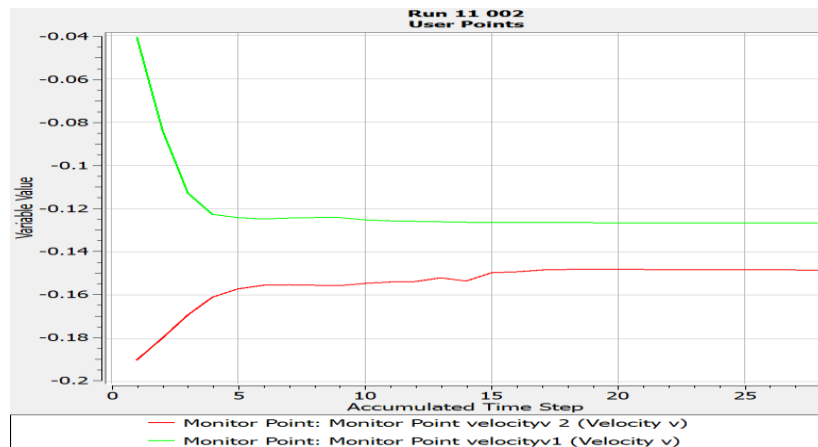
Figure 47: Convergence of the lateral velocity for the non-deformed mesh simulation containing 3472 nodes

## 7.2 Mesh independence study

Although a good mesh quality is achieved and the solution converges based on RMS residual values, monitor points and imbalances, it is essential to check that the obtained results are independent of the mesh resolution. Therefore, a mesh independence study has to be carried out.

Once the convergence criteria are met, (convergence of RMS residual error to 10^{-4}, monitor points are steady and imbalances below 1%), the global mesh has to be further refined in order to achieve finer cells throughout the domain.

If the convergence criteria are accomplished, the monitor point values from the actual simulation are compared to the last simulation values. If they are the same, within the allowable tolerance, then the previous mesh was accurate enough to capture the result. At this point, mesh independence is considered to be achieved.

In other words, the mesh independence study consists of comparing the output of two different mesh simulations. The output of this particular case is the lateral forces affecting the FA structure. In this case, the mesh with the smallest density achieving mesh independent solutions should be used to reduce computational expense.

If the actual monitoring values are not within the acceptable tolerance range, the solution will not yet be independent of the mesh. Since the obtained solution is changing because of the mesh resolution, the refinement process will have to be repeated until an independent mesh size solution is achieved.

7.3 Deviation measurement

In this thesis, meshes with different node densities are created to simulate the behavior of a FA row towards bow. Table 2 includes the features of the mentioned meshes and the refinement strategy followed to create them. Note that the mesh node density represents the number of nodes contained in each Fuel Assembly, not in the whole mesh.

The aim of creating meshes with different node densities is to determine which mesh will best enable the most efficient, but still accurate, estimation of the lateral hydrodynamic forces inside the reactor core. Within this section, the lateral hydrodynamic forces obtained from the simulations with different mesh resolutions are compared for the non-deformed and the C-shape deformed structure using the four following approaches:

- Root Mean Square Error
- Averaged Root Mean Square Error
- Averaged Mean Absolute Error
- Quadratic Mean Relative Error

The aim is to determine the most reasonable deviation measure for the mesh independence study.

7.3.1 Root Mean Square Error

The Root Mean Square Error (RMSE) is a fundamental measure of deviation, as it directly quantifies the goodness of fit between two datasets. In the present study, the main objective is to determine the influence of the lateral forces on FA bowing. Therefore, the RMSE values are generated by comparing the transversal forces of the different subdomains of two different mesh simulations. In this thesis, the output from the finer mesh is always taken as the predicted reference value and the forces from the coarser mesh as the observed value.

$$\text{RMSE} = \sqrt{\frac{1}{N}\sum_{i=1}^{N}(X_{O,i} - X_{P,i})^2}$$

(0-1)

Setting "N" as total number of data compared, "X_P" as the predicted values and "X_O" as the observed values. Figure 48 represents the RMSE value of the lateral forces between the different simulations

.
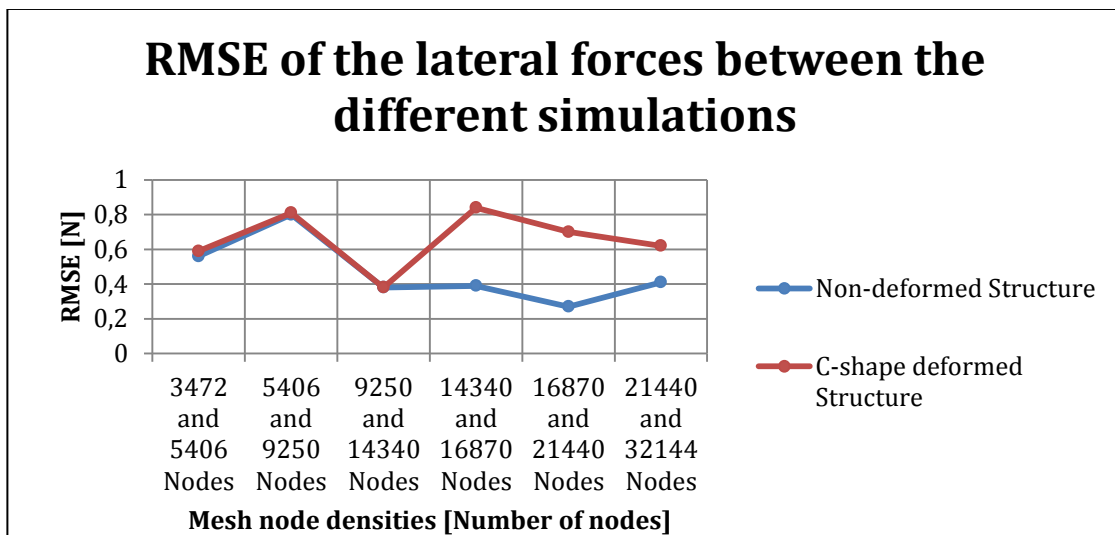
Figure 48: RMSE of the lateral forces between the different simulations

7.3.2 Averaged Root Mean Square Error

In cases where the data range is very wide, the RMSE is likely to be affected by the width of the data range, which would hamper comparisons. A very wide data range can be observed for the lateral hydraulic forces within the domain (Figure 49).
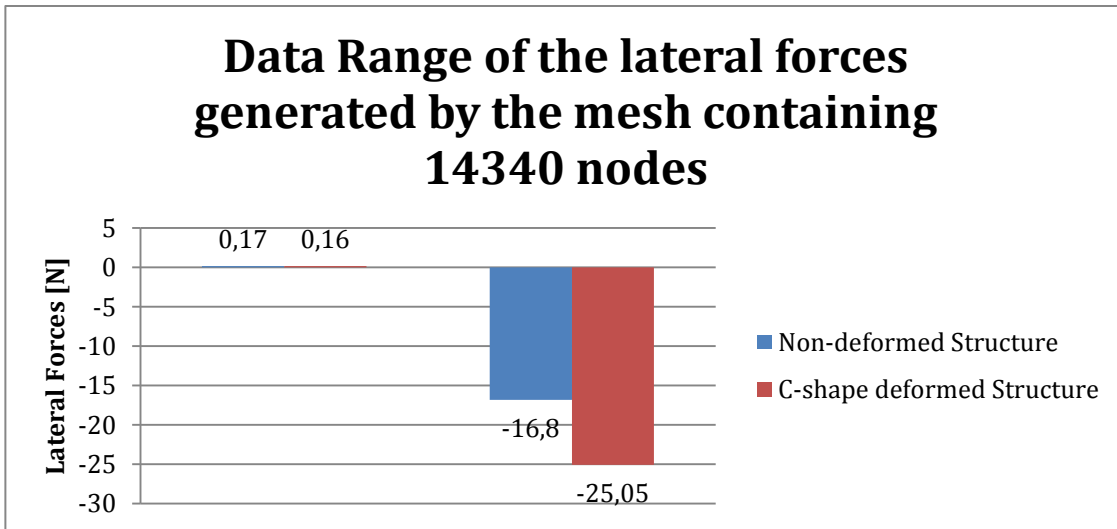
Figure 49: Data range of the forces generated by the mesh containing 14340 nodes

Note that the negative sign preceding the maximal lateral force value indicates the direction of this force (from the FA region in contact with the wall to the center of the FA row). From the fluid mechanics point of view, the velocity of the flow close to the boundary layer is very low, hence, the lateral forces are relatively small over the FA next to the outer boundary due to the presence of the wall. That is the reason for such a wide data range concerning the lateral forces. The width of the data range makes it reasonable to normalize the RMSE value with reference to the average value of the dataset.

$$\text{ARMSE} = 100 * \frac{\sqrt{\frac{1}{N}\sum_{i=1}^{N}(X_{O,i} - X_{P,i})^2}}{X_{average}} \tag{0-2}$$

Figure 50 depicts the RMSE and the ARMSE values obtained after comparing the lateral forces generated by the different mesh simulations.
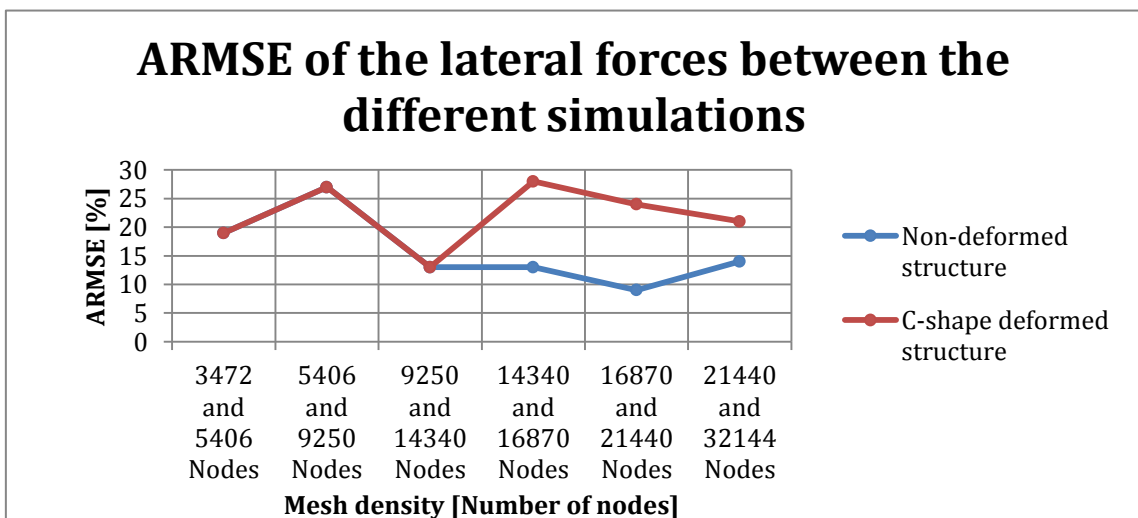
Figure 50: ARMSE of the lateral forces between the different simulations

7.3.3 Averaged Mean Absolute Error

The Averaged Mean Absolute Error (AMAE) approach calculates the relative deviation between the two datasets and divides it by the average value of the reference dataset. Figure 51 contains the AMAE values obtained after comparing the lateral forces generated by the different mesh simulations.

$$AMAE \; [\%] = \frac{100}{N} * \sum_{i=1}^{N} \left\{ \left\| \frac{X_{O,i} - X_{P,i}}{X_{P\_average}} \right\| \right\} \qquad (0\text{-}3)$$
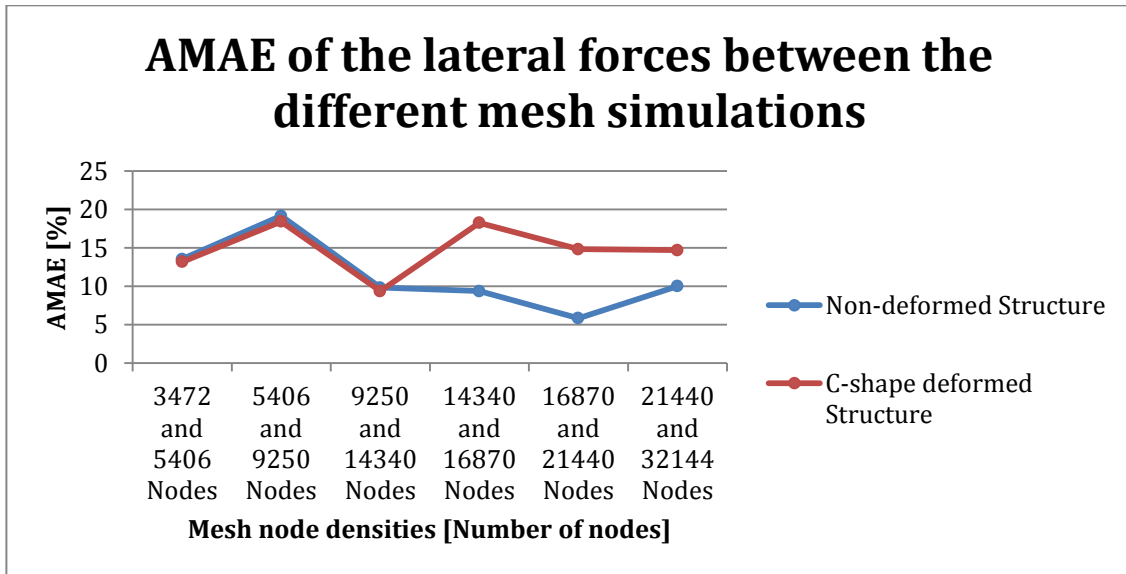
Figure 51: AMAE obtained values after comparing the lateral forces generated by the different mesh simulations

7.3.4 Quadratic Mean

The Quadratic Mean (QM) value does not quantify the goodness of fit between two datasets. Instead, the QM represents the equivalent force throughout the domain which produces FA deformation.

$$Quadratic \; Mean \; = \sqrt{\frac{1}{N} \left(\sum_{i=1}^{N} X_i^2 \right)} \qquad (0\text{-}4)$$

The relative error of the Quadratic Mean values generated by the simulations is calculated in order to determine the difference in the outputs of the different meshes.

$$\text{QM relative error } [\%] = 100 * \left\| \frac{\sqrt{\frac{1}{N}\left(\sum_{i=1}^{N} X_{P,i}^2\right)} - \sqrt{\frac{1}{N}\left(\sum_{i=1}^{N} X_{O,i}^2\right)}}{\sqrt{\frac{1}{N}\left(\sum_{i=1}^{N} X_{P,i}^2\right)}} \right\| \qquad (0\text{-}5)$$

Figure 52 represents the QM relative error values obtained after comparing the lateral forces generated by the different mesh simulations.
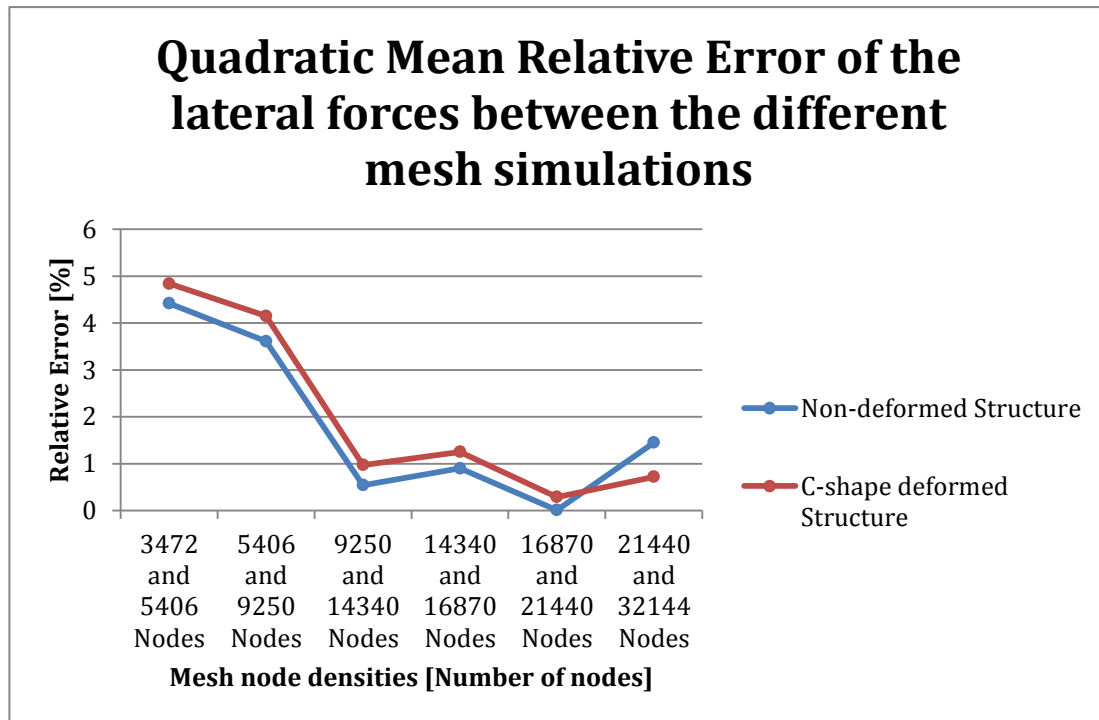
Figure 52: Quadratic Mean relative error values after comparing the values of the lateral forces generated by the different mesh simulations

Despite being commonly used to measure the differences between two datasets, neither the ARMSE nor the AMAE approaches measure the deformation changes in the FA according to our needs.

The force distribution changes in the core as the mesh is further refined. Using these approaches as a reference to measure mesh independence may lead to wrong conclusions, as they take into account all local force changes between the compared datasets. Although little force variations may have no globally visible impact on the FA structure, the local ARMSE and AMAE value changes, indicating that both meshes generate different results.

This can be observed by analyzing the difference between the QM relative error, the ARMSE and the AMAE of the meshes containing 14340 and 16870 nodes. Comparing the lateral forces for the non-deformed structure simulation, the QM value differs 0.89%, indicating the equivalent force inducing FA bow barely changes with increasing mesh density (Figure 52). On

the other hand, the ARMSE of the transversal forces equals to 13% (Figure 50), while the AMAE approach determines a deviation of 9.3% between both datasets (Figure 51).

This is the reason why in this thesis, the QM value is used as reference for the mesh independence study, as it is not influenced by the locally different force distribution within the domain.

7.4 Mesh Independence approaches

7.4.1 Simulation under conditions of no structural deformation

Figure 53 represents the mesh density, measured in amount of nodes, against the Quadratic Mean value of its outputs, hence, the resulting transversal forces.
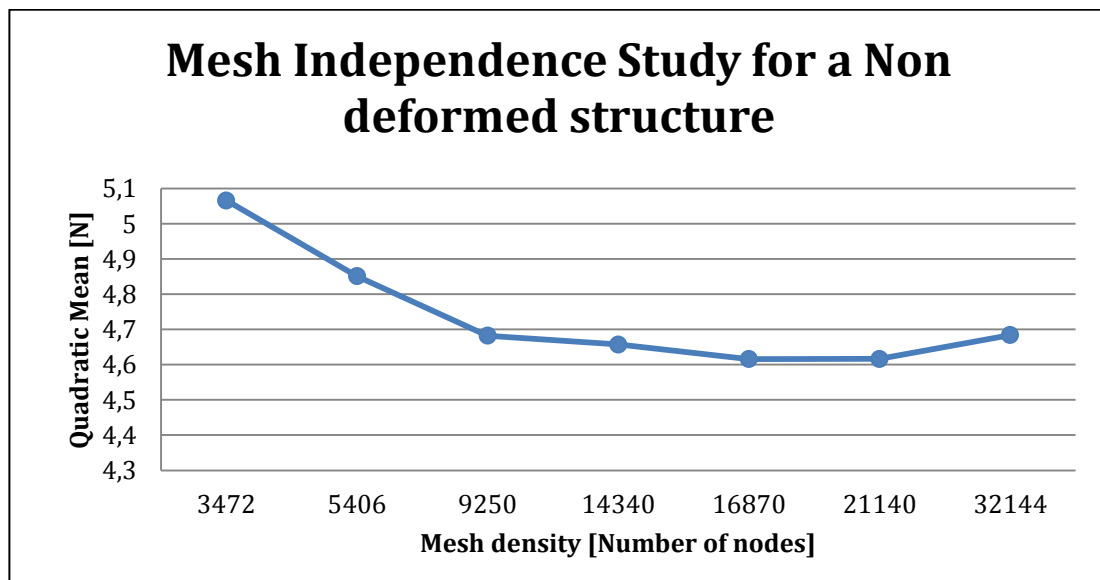
Figure 53: Mesh independence study for a non-deformed Fuel Assembly row

The coarsest mesh generated, consisting of 3472 nodes, is globally refined in order to obtain finer cells throughout the domain.

Comparing the QM values of the first two simulations, it is obvious that the solution is changing due to mesh resolution, thus, the solution is not yet independent of the mesh. The node density has to be further increased and the comparison of the output done, until a mesh independent solution is achieved.

According to the plot above, the coarsest mesh which would accurately capture the result is the one containing 9250 nodes. Although this mesh is further refined, the QM values vary within an acceptable tolerance of less than 1.5 %. At this point, mesh independence is considered to be achieved.

As stated in section 7.2, in order to reduce computational expense, the coarsest mesh giving mesh independent solutions is chosen, thus the mesh containing 9250 nodes.

7.4.2 Simulation under C-shaped structural deformation

Figure 54 shows plots the successive meshes with increasing number of nodes against the Quadratic Mean of the lateral hydrodynamic forces obtained after simulation.
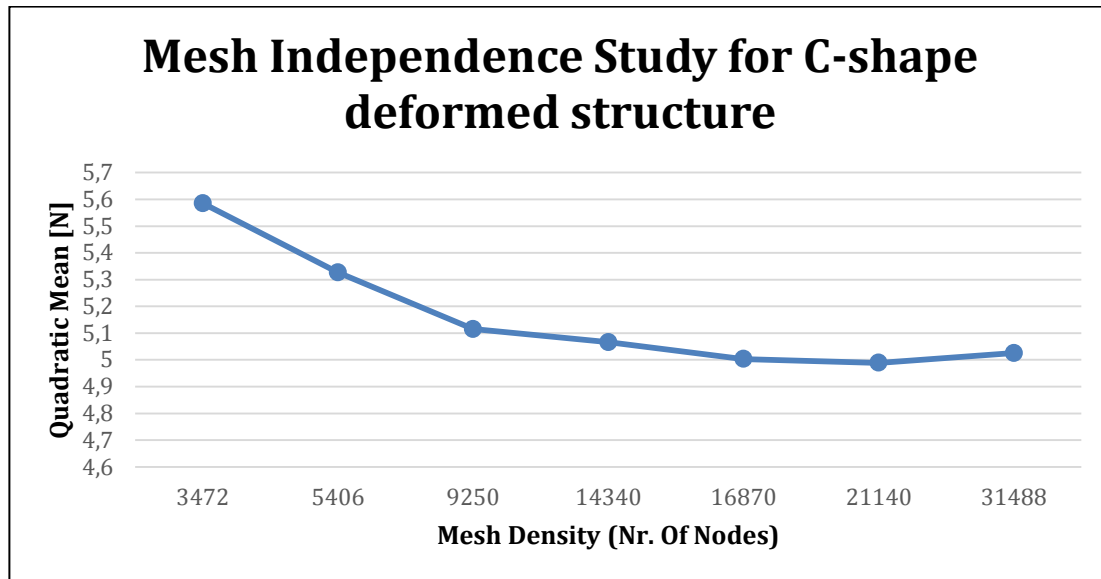
Figure 54: Mesh independence study for a C-shape deformed FA row

The same meshes as for the simulation without structural deformation are used to produce the evaluated results. Again, a range of tolerance of approximately 1.5% in the QM value is admitted.

This time, the coarsest mesh achieving mesh independent results is the one containing 14340 nodes.

7.4.3 Tolerance acceptance and analysis conclusion

The values of the force distribution, measured by the QM approach, are mesh-independent in a 98.56% (1.44% deviation between the force distribution generated by the simulation with a mesh resolution of 9250 Nodes and 21140 Nodes).

The porous model contains uncertainty regarding some of its input parameters and initial assumptions, which can cause a deviation higher than a 1.5% in the simulation results.

The inlet conditions, such as the inlet velocity profile, have been assumed under a certain degree of uncertainty. Moreover, the force distribution inside the core is very sensitive to mesh changes in the "critical regions". As mentioned in section 5.1.2 **¡Error! No se encuentra el origen de la referencia.**the critical regions are the areas surrounding the gaps between the

Fuel Assemblies, the core inlet and outlet and the transition between rods and grids. This means, rapid solution variation takes place in these regions as mesh density changes.

When creating the mesh in ANSYS ICEM CFD, the selected values for "axial and lateral node spacing" will have great influence on the obtained output. The mesh consisting of 14340 nodes is simulated under conditions of no structural deformation with two different lateral node spacing sizes. A sensitivity analysis is performed using the ARMSE approach to determine the impact of different node spacing sizes on the lateral force distribution within the domain. The obtained results are represented in Table 5.

Table 5: Analysis of the influence of lateral node spacing size on the simulation output

Lateral node spacing size	ARMSE non-deformed structure [%]
0.001 m and 0.005 m	12.746511

The magnitude of the ARMSE indicates a variation in the mesh resolution near the gap region will have considerable influence on the obtained results.

The same approach is also used to evaluate the influence of different axial node spacing sizes on the lateral force distribution. In this case, the mesh containing 21140 nodes is simulated assuming no structural deformation with two different axial spacing sizes   (Table 6).

Table 6: Analysis of the influence of axial node spacing size on the simulation output

Axial node spacing size	ARMSE non-deformed structure [%]
0.005 m and 0.01 m	2.489758

The ARMSE value shows the force distribution within the porous model varies slightly with different axial node spacing sizes.

The tables above indicate that the model's most critical region is located next to the gaps and will hence require a much finer mesh than the rest of the domain.

The outcome of the lateral hydraulic forces requires further analysis concerning the "criticality" of inlet and outlet core regions. Therefore, the transversal forces generated after simulation with the meshes containing 16870 and 14340 nodes were compared.

As stated in section 7.4.1, both meshes do almost generate the same force distribution, nevertheless, the values of lateral forces experience large deviations in some regions depending on the selected mesh. Figure 55 depicts the average relative lateral force deviation along the FA row.
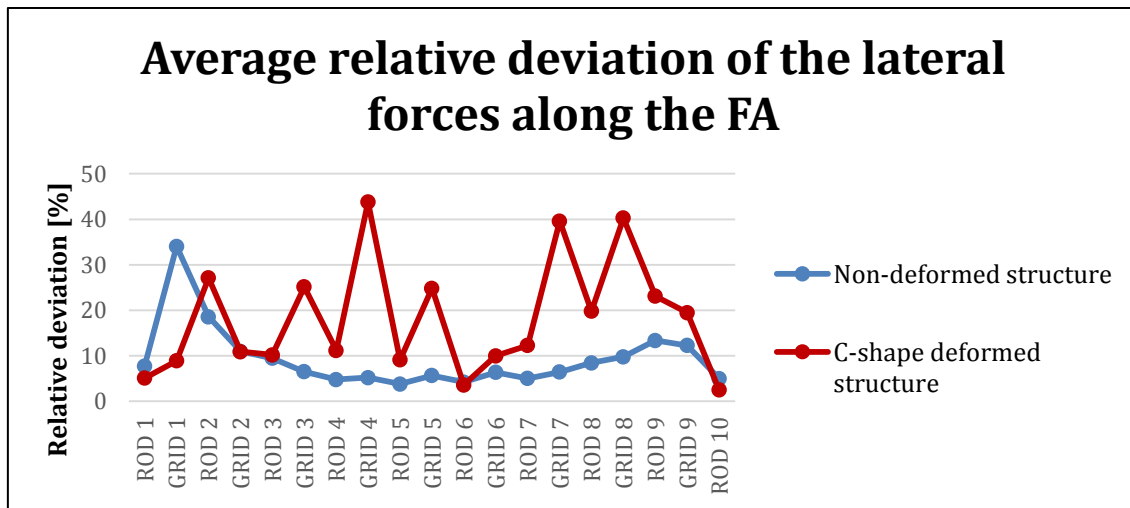
Figure 55: Average relative deviation of the lateral hydrodynamic forces from meshes containing 14340 and 16870 nodes

For the non-deformed structure, rods 2 and 9 and grids 1, 2, 8 and 9 present a remarkably high deviation in their results.

On the other hand, the lateral forces obtained after simulating the C-shape deformed structure differ considerably for rods 2, 8 and 9, as well as for grids 4, 7 and 8.

The plot above reinforces the initial supposition, that the mesh density at the inlet and outlet regions has a great influence on the simulation output. These are also the areas where the lateral hydrodynamic forces are maximal. Based on Figure 55, the fuel rods and the grids close to the inlet and outlet of the core are considered critical regions. In order to achieve accurate results, the amount of nodes in these areas is increased in comparison with the rest of the domain.

It is important to notice that, under conditions of C-shape structure deformation, the output value deviation is generally higher concerning the spacer grids than the rods. The fact, that much higher deviations are obtained in the grids than in the rods for the C-shape deformed structure lies beyond the scope of this thesis and should be further investigated in the future.

Assuming the mentioned factors to have a certain influence on the force distribution makes the obtained mesh independence study valid, as a 1.5% deviation is very low taking into account the uncertainty surrounding implementation and simulation of the present porous model.

In summary, the mesh which would accomplish the requirements of accuracy and low computational cost for the porous model under conditions of C-shape and non-structural deformation would be the mesh consisting of 14340 nodes. In the case of the non-deformed structure, a coarser mesh would also fulfill the desired accuracy. Nevertheless the simulation of the C-shaped deformed FA needs this mesh density to ensure the captured result is mesh-independent.

8. Conclusion and outlook

The objective of this work was to carry out an optimization study of a 2D CFD porous model in order to determine which mesh would best enable the most efficient, whilst still accurate, estimation of the lateral hydrodynamic forces generated by the coolant flow inside the core. An accurate estimation of the lateral forces can help to better predict the mechanical behavior of the Fuel Assemblies towards bow and prevent possible safety and operational problems in nuclear power plants. Simulating the hydraulics and mechanics of a resolved PWR reactor core would be excessively computationally expensive. Instead, a porous model with a porosity of similar characteristics is constructed in order to make the simulation feasible.

To reduce computational expense, only one FA row containing 16 Fuel Assemblies was considered. The model size was further reduced assuming symmetry along the middle of the row, hence simulating only 8 Fuel Assemblies.

The geometry and meshes with different node densities were generated for a single FA using ANSYS ICEM CFD. The FA row was created by reproducing 7 times the mentioned mesh and simulated under conditions of C-shape and non-structural deformation to determine the lateral force distribution inside the core. The aim of comparing the results from both study cases is to determine whether the condition of structural deformation had an influence on the results of the study and on the convergence of the simulations.

From the convergence point of view, the simulation's Residual RMS Error values were reduced to an acceptable value and the solution imbalances were lower than 1%. Furthermore, monitoring points were placed to track the value of the lateral velocity at the locations where it reached a relatively high value. Lateral coolant flow velocity is directly related to the lateral forces, which are the main cause of FA deformation. The fact that this parameter reached a steady solution confirmed the validity of the obtained solution.

Based on the geometry of this model, it was assumed that the core inlet and outlet, the transition regions between fuel rods and spacer grids, as well as the regions in contact with the gaps, would present faster variation in their simulation output values, hence requiring a higher node density than the rest of the domain. Mesh refinement strategy was especially focused on increasing the cell density in the areas next to the gaps.

A mesh independence study was performed in order to evaluate which mesh resolution could accurately capture the force distribution within the core while accomplishing the requirement of low computational cost.

To evaluate the impact caused by the lateral hydrodynamic forces on the FA structure, the Quadratic Mean (QM) approach was used as a reference for the mesh independence study, as it is not influenced by the locally different force distribution within the domain. The porous model implementation contained uncertainty regarding its input parameters and initial assumptions, such as the inlet velocity profile. In addition, it was demonstrated that the lateral

force distribution is very sensitive towards mesh density changes in the regions in contact with the gaps.

Assuming the mentioned factors to have a certain influence on the force distribution, a tolerance range of 1.5% in the QM values was accepted. At this point, mesh independence was considered to be achieved.

Finally, based on the mesh independence study results, the requirements of accuracy and low computational expense were better accomplished for both study cases by the mesh consisting of 14340 nodes. Although this mesh is further refined, the QM values vary within an acceptable tolerance of less than 1.5 %. At the same time, convergence was also achieved within a similar amount of iterations.

Based on the fact that the coolant flow has a strong impact on the structure, and vice-versa, the mentioned mesh can be used in future studies to implement a Fluid Structure Interaction (FSI) interface, which couples the distribution of the lateral hydraulic forces on each Fuel Assembly with its mechanical behavior. This could be used to determine the effect of lateral hydraulic forces on the Fuel Assembly core structure, and thus to predict FA bow.

In this thesis, fourth order polynomial velocity profiles were assumed at the inlet and outlet boundary regions. Further study of the FA behavior with different profiles would be interesting, as the mentioned assumption is an approximation of the real life operating conditions inside the core.

The present model is simulated under isothermal heat transfer conditions. In reality, heat is released inside the core. This could be represented by introducing a volumetric heat source in the CFD model. In this case, the equation of conservation of energy should also be solved, leading to more computational cost.

The present study is performed for a 2-D CFD porous model. A 3-Dimensional representation of the Fuel Assembly row would also be a possible object of study, though deriving in great computational expense.

Appendix

Mesh of the entire fuel assembly row
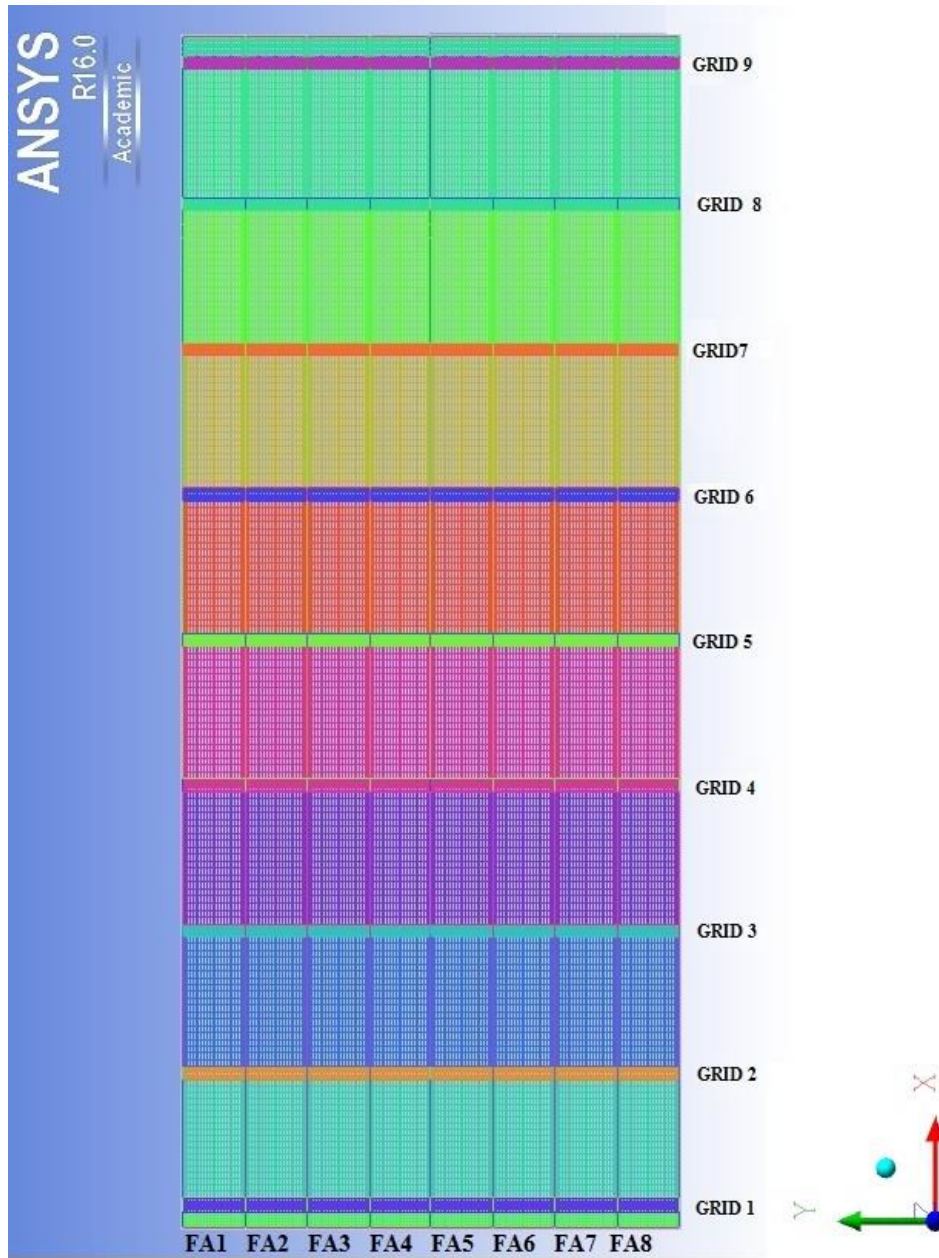

Figure 56: Mesh of the entire Fuel Assembly row

Bibliography

[1]   A. Wanninger, M. Seidl, and R. Macián-juan, "UNDERSTANDING FUTURE RESEARCH
        NEEDS TO BETTER DESCRIBE FUEL ASSEMBLY BOW IN PWRs," *45th Jahrestagung
        Kerntechnik*, 2014.

[2]   S. Y. Jeon, N. G. Park, Y. K. Jang, J. M. Suh, and K. L. Jeon, "An Investigation on the Bow
        Characteristics of the PWR Fuel Assembly," *Trans. Korean Nucl. Soc. Autumn Meet.
        Gyeongju, Korea*, pp. 247–248, 2011.

[3]   C. J. Lascar, "ADVANCED PREDICTIVE TOOL FOR FUEL ASSEMBLY BOW BASED ON A 3D
        COUPLED FSI APPROACH," *Topfuel Conf. Proc.*, 2014.

[4]   J. . Peybernès, "EVALUATION OF THE FORCES GENERATED BY CROSS-FLOW ON PWR
        FUEL ASSEMBLY," *Struct. Behav. fuel Assem. water Cool. React. Proc. a Tech. Meet.*, pp.
        13–21, 1986.

[5]   R. Macián-juan, "Lecture 1: Nuclear power reactor systems," in *Thermal-hydrualics
        analysis of nuclear systems*, 2014.

[6]   G. Kessler, A. Veser, F.-H. Schlüter, W. Raskob, C. Landman, and J. Päsler-Sauer, *The
        Risks of Nuclear Energy Technology*. 2014.

[7]   R. Macián-juan, "Lecture 6: Thermal-hydraulic Analysis of Nuclear Reactors," in
        Thermal-hydrualics analysis of nuclear systems, 2014.

[8]   M. Chelbi, "Construction of a 2D CFD Model for the Analysis of Steady-state Axial and
        Lateral Hydraulic Forces in a PWR Reactor Core Based on a Porous Medium Approach,"
        2015.

[9]   J. Yan, Y. Zhang, B. Yang, W. Li, and Y. Zhou, "Influence of Spacer Grid Outer Strap on
        Fuel Assembly Thermal Hydraulic Performance," *Sci. Technol. Nucl. Install.*, vol. 2014,
        2014.

[10]   K. Song and S. Lee, "Effect of Weld Properties on the Crush Strength of the PWR Spacer
        Grid," *Sci. Technol. Nucl. Install.*, vol. 2012, pp. 1–12, 2012.

[11]   A. Wanninger, "Development of Computational Methods to Describe the In-Reactor
        Mechanical Behavior of PWR Fuel Assemblies," 2015.

[12]   A. Stabel, J. Horvath, "Advanced Methodology To Predict in Reactor Bow of Pwr Fuel
        Assemblies for Efficient Design Optimization : Background , Validation , Examples,"
        Nucl. Eng. Des., pp. 1–12, 2011.

[13]   Z. Karoutas, E. Baglietto, R. Brewster, and E. Volpenhein, "Evaluating PWR Fuel
         Performance Using Vessel CFD Analysis," *Proc. 2010 LWR Fuel Perform.*, pp. 684–885.

[14]   Roache, P. J. (1997). Quantification of uncertainty in computational fluid dynamics.
Annual Review of Fluid Mechanics, *29*(1), 123-160.

[15] AIAA, "Guide for the Verification and Validation of Computational Fluid Dynamics
Simulations," American Institute of Aeronautics and Astronautics, AIAA-G-077-1998, Reston,
VA, 1998.

[16] Oberkampf, W. L., & Trucano, T. G. (2002). Verification and validation in computational
fluid dynamics. *Progress in Aerospace Sciences*, *38*(3), 209-27

THESIS BUDGET

1 Budget breakdown

This section contains the numerical estimation of the costs derived from the completion of this Master Thesis. They have been divided in three different sections:

- Manpower: Salaries & time employed to carry out this project.
- Equipment: Hardware and software used for this Thesis
- General expenses: Heating, lighting & electricity consumption

1.1 Workforce

The main contributors to this section are:

1) Full-time dedication of the master student to accomplish the research project, for a period of seven months.
2) Part-time dedication of the TUM Engineer Researcher from the "Lehrstuhl für Nukleartechnik", dedicating a about 4 hours a week for guiding and mentoring of the master´s student.

1.2 Equipment

The equipment used for this research project can be divided in two different areas:

1) The physical equipment (CPU, screen, keyboard, etc.)
2) The programs used for simulation and analysis (e. g. ANSYS CFX, ANSYS CFD, etc.)

For the allocation of the equipment costs, its acquisition value and its operating life and amortization are taken into account. The amortization cost is calculated as follows:

$$Amortization\ cost = \frac{A \cdot t \cdot L}{T}$$

Being:

A: acquisition cost of the equipment (€).

L: usage level of the equipment.

t: usage time of the equipment for this project

T: total operating life of the equipment.

1.3 General expenses

This area includes all costs incurred to make the research of the student possible, mainly electricity for lighting and make the computers run and heating costs.

2 Budget

This section contains the breakdown and explanation of the three main cost sections mentioned before.

2.2 Workforce

The two main contributors must be first be classified according to their education level in order to accurately estimate the costs related to their dedication to this project.

The senior mechanical engineer is a PhD researcher working for "Lehrstuhl für Nukleartechnik TUM" (nuclear energy department).

The Master student is a graduate engineer working as a HIWI student for the nuclear energy department. The HIWI program ("Hilfswillinge") offers students the opportunity to work for a department as assistant scientists.

The following working conditions have been considered:

- 12 salaries per year.
- Both workers will have 30 days of vacation per year
- Working full-time, a Graduate Mechanical engineer under the HIWI program will have at least a net salary of 700 €/month.
- A senior Mechanical engineer in Germany will have a net salary of 2800 €/month.
- Contribution for hiring a graduate mechanical engineer by the department of Nuclear Energy:
    - Health insurance 8,3%.
    - Taxes (IRPF) 18%.
    - Liability for the company to pay during the vacation period 0,6%
- Employer taxes 5%.
- Diets: 5 €/working day.

The total hours worked will be:

	Monthly working Hours	Working period (months)	Dedication	Total Hours Worked
Graduate engineer	160	7	100%	1120
Senior engineer	160	7	10%	112

Budget Table 1: Total workforce hours.

Hence, the cost for the Department of Nuclear energy of the Graduate engineer is:

Concept	Cost (€/Month)
Net Salary	720,4
Health insurance	100
Taxes (IRPF)	216
vacations	163,636364
gross salary	1200
Employer taxes	60
Fringe (Diets)	100
TOTAL Cost of a graduate engineer for a period of 7 months	**9520 €**

Budget Table 2: Cost of the graduate engineer.

The cost of the senior engineer with a 10% dedication for the department (4 hours/week):

Concept	Amount (€/month)
Net Salary	2800
Health insurance	233,3
Taxes (IRPF)	504
vacations	381,82
gross salary	3919,2
Employer taxes	195,96
Fringe (Diets)	100
TOTAL COST in 7 months	29505,8 €
Total Cost senior engineer under 10% dedication for a period of 7 months	**2950,6 €**

Budget Table 3: Cost of the senior engineer.

2.3 Equipment

The amortization costs of the equipment used for this project are:

Equipment name	Cost of aquisition (€/unit)	Useful Lifetime (years)	Usage Time (h)	Usage Level	Amortization Cost (€)
PC - HP Z440	1886,39	4	900	100%	225
ANSYS CFX Software – academical license	1556,9	2	600	85%	255
				Total	**480 €**

Budget Table 4: Equipment devaluation costs

2.4 General expenses

The expenses associated to light and water used during the thesis completion must also be included in the investment budget. These expenses were mainly due to heating costs, specially high due to the low temperatures in Munich during the winter and spring months, lightning the computer room and electricity used by the computers. The following assumptions have been made:

The cost of electrical consumption is considered to be 0,15 €/Kwh.

Two heaters consuming 5 KWh, during almost the whole working shift (160 h/month).

PC - HP Z440 consumption is 0,4 KWh

Electric consumption by the lightbulbs is 1 KWh

Devaluation of the lightbulbs and heaters will not be taken into account.

Material	Electrical consumption (Kwh)	Total Energy Cost (€)
2 Heaters	5	120
Computer	0,4	9,6
Lighting (10 lightbulbs)	5	24
	Total Cost per month	153,6
	Total Energy costs (7 Month Period	1075,2 €

Budget Table 5: General expenses

2.5 Material Budget and Investment Budget

The material budget is obtained after adding the costs of workforce, equipment and general expenses. The investment budget, which is the real cost of the whole project, is obtained once the 21% VAT (Value Added Tax) is added to the material budget.

Concept	Total Cost (€)
Workforce	12.470,60 €
Equipment	480 €
General Expenses	1075,2 €
MB (Material Budget)	**14.025,77 €**
VAT(21%)	2.734,61 €
Total Investment Budget	**16.971 €**

Budget Table 6:Investment Project Budget.

The total investment budget for the Master Thesis "Optimization study of a 2D CFD Porous Model for the Fluid-Structure Coupling of PWR Fuel Assemblies in the Reactor Core" is:

Sixteen thousand nine hundred and seventy-one Euros

Valencia, September 2017.

Signed: Luis Rafecas Caballero